Analytical Modeling of Bulk Heterojunction Organic Solar Cells Incorporating Spatial Distribution of Photocarrier Generation

A thesis submitted to the
Department of Electrical and Electronic Engineering (EEE)
of
Bangladesh University of Engineering and Technology (BUET)

In partial fulfillment of the requirement for the degree of
MASTER OF SCIENCE IN ELECTRICAL AND ELECTRONIC ENGINEERING

by

Mokter Mahmud Chowdhury

(Roll No.: 0412062246)

DEPARTMENT OF ELECTRICAL AND ELECTRONIC ENGINEERING (EEE)
BANGLADESH UNIVERSITY OF ENGINEERING AND TECHNOLOGY (BUET)

JUNE 2015

The thesis titled "**Analytical Modeling of Bulk Heterojunction Organic Solar Cells Incorporating Spatial Distribution of Photocarrier Generation**" submitted by Mokter Mahmud Chowdhury, Roll No.: 0412062246 F, Session: April 2012, has been accepted as satisfactory in partial fulfillment of the requirement for the degree of MASTER OF SCIENCE IN ELECTRICAL AND ELECTRONIC ENGINEERING on June 21, 2015.

Board of Examiners

---

1. Dr. Md. Kawsar Alam — Chairman (Supervisor)

Assistant Professor
Department of Electrical & Electronic Engineering (EEE)
BUET, Dhaka-1000, Bangladesh

---

2. Dr. Taifur Ahmed Chowdhury — Member (Ex-officio)

Professor and Head
Department of Electrical & Electronic Engineering (EEE)
BUET, Dhaka-1000, Bangladesh

---

3. Dr. Md. Ziaur Rahman Khan — Member

Professor
Department of Electrical & Electronic Engineering (EEE)
BUET, Dhaka-1000, Bangladesh

---

4. Dr. Muhibul Haque Bhuyan — Member (External)

Professor and Chairperson
Department of Electrical & Electronic Engineering (EEE)
Green University of Bangladesh, Dhaka-1216

Declaration

It is hereby declared that this thesis or any part of it has not been submitted elsewhere for the award of any degree or diploma.

Signature of the candidate

_____

Mokter Mahmud Chowdhury

(Roll No.: 0412062246)

Dedication

to my Creator

Acknowledgements

I would like to express my indebtedness and deep sense of gratitude to my thesis supervisor Dr. Md. Kawsar Alam, Assistant Professor of the Department of Electrical and Electronic Engineering, Bangladesh University of Engineering and Technology, Dhaka for his unique guidance, insightful suggestions, beyond comparable encouragement and help all along the course of this work. His enthusiasm, dedication and friendly attitude provided the perfect balance of guidance and freedom. His extraordinary passion for research has always deeply inspired me. My very special gratitude goes to him for spending many hours discussing about our research works, from which I have learnt a lot. I am also grateful to him for acquainting me with the world of advanced research and giving me the courage to explore it passionately as well. It was a great honor and pleasure to be a part of his research group, and it will always be.

I also thank the members of my thesis committee, Prof. Dr. Taifur Ahmed Chowdhury, Prof. Dr. Md. Ziaur Rahman Khan and Prof. Dr. Muhibul Haque Bhuyan, for their invaluable feedback on my work.

In addition, I express my sincere gratitude to all of the faculty members for their continuous guidance and helpful instructions through the entire B.Sc. and M.Sc. programs, which has made me capable to complete this thesis successfully. My special thanks goes to Prof. Dr. M. M. Shahidul Hassan who introduced me to the field of device modeling in my undergraduate research career. I am also grateful to Prof. Dr. Md. Ziaur Rahman Khan for his constant support and encouragement toward my research works.

My cordial thanks goes to my family members for their unconditional support, kindness and tolerance toward my eccentric way of life. Without their support, it would be impossible to continue my study and research works.

Finally and most importantly, I would like to express boundless gratitude to my Almighty Creator for giving me the opportunity, strength, skill and courage to complete this thesis.

Abstract

This thesis presents an optoelectronic analytical model for bulk heterojunction organic solar cells. Incorporating optical transfer matrix theory in the electrical transport equations, we combine optical and electrical phenomena. This leads us to a single unified expression of current-voltage characteristic which considers the position and wavelength dependent carrier generation rate. Spatial distribution of the carrier generation rate is considered rigorously unlike previous analytical models. The model is capable of considering the optical propagation through the device structure as well as the optical phenomena such as reflections and interference effects. We verify the model with numerical results and published experimental data. We find that the consideration of spatial distribution of photocarrier generation rate is important to predict the device performance accurately.

In addition, an analytical model for bulk heterojunction organic solar cells is developed on the basis of empirical expression of carrier generation rate. By developing the empirical formula and incorporating in the carrier transport equations, we successfully bring in the spatial distribution effect of generation rate into the current-voltage (*J-V*) characteristic of this solar cell. The proposed empirical formula helps us to derive the *J-V* curve expression, especially for the cases where carrier generation rate cannot be described by any physics-based closed form expression, and the spatial distribution of the generation rate profile to be extracted and used directly from published/available data. We justify our model by comparing with numerical simulations and published data. We observe that this model is capable of considering position dependency of carrier generation rate in a very simple and straightforward way.

Table of Contents

List of Figures

List of Tables

Chapter 1

Introduction

The increasing demand for energy over the past fifty years has resulted in a drive for research into possible energy sources that are both commercially viable and do not create waste products that are detrimental to the environment [1]. It has been projected that, by 2050, worldwide energy consumption will increase to approximately 28 TW, from its 2006 level of around 11 TW [2]. With a potential of approximately 100000 TW, the solar energy that reaches the Earth's surface is the largest carbon-free energy source, which could be harvested with photovoltaic devices [2].

The economic and social dimensions of the present climate change are threatening. According to the Intergovernmental Panel on Climate Change Assessment, global carbon dioxide emissions have risen by 3.3% per year since 1950, average global temperatures have increased from 0.3° C to 0.6° C since the late 1800's, and recent years have been among the warmest since the 1860's [3]. The average global temperature is likely to rise by 2° C during the next century (range: 1° to 3.5° C), and in the same period the sea level is expected to rise by 50 cm [4]. The emission levels of carbon dioxide that we generate by the constant use of fossil fuel are literally killing our planet. The usage of solar energy will only provide us with a clean environment, a life where we will not have to constantly worry about the ever so reducing resources to provide us with the basic comforts of our life.

Apart from environmental concerns, several authors state that implementing renewable, carbon-emission free energy techniques are of great economic value. Today's dominant power supply system is centralized, large-scale, and focused on increasing consumption. Its successor could be decentralized, downsized and directed toward meeting demand [5]. The forthcoming decentralized energy mix will be supplied by small modular generation units such as combined-cycle gas turbines,

wind turbines, photovoltaic panels and fuel cells. Electricity from large power plants will soon prove too expensive for it to maintain its traditional dominant role. So creating the use of solar energy seems to be one of the best options available. And, the most direct use of solar energy is the conversion of photons to electricity by the photovoltaic effect [2].

1.1 Historical Background and Generations of Solar Cell Technology

Many early experiments have reported about the phenomenon of photovoltaic effect. Among them, the experiment of Alexandre-Edmond Becquerel, in 1839, is the most well known [6]. In 1883, the first solar cell was built, by Charles Fritts, who coated the semiconductor selenium with an extremely thin layer of gold to form the junctions. The device was only around 1% efficient. The modern age of solar power technology arrived in 1954 when Bell Laboratories [7], experimenting with semiconductors, accidentally found that silicon doped with certain impurities was very sensitive to light. And, eventually, the first solar cell was made by Daryl Chapin, Calvin Fuller, and Gerald Pearson at Bell laboratories utilizing a silicon p-n junction to achieve 6 % conversion efficiency [7]. This milestone created interest in producing and launching a geostationary communications satellite by providing a viable power supply. As a result, with the space age, a market for solar cells emerged and the first American satellite Vanguard I launched in 1958 equipped with six solar cells mounted on the body. The use of solar cells on the satellite was found to be successful and the power-to-weight ratio of solar cells ensured their further success for space applications. For the initial history of solar cells their prices were dictated by the semiconductor industry. The estimated price had reached $100 per watt by 1971. Since then progress have been massive. Solar cells are now part of a global industry. According to a study by the European Wind Energy Association (EWEA), within the energy sector in Europe, photovoltaics accounted for the largest share of new installations. In 2011, 21,000 MW worth of capacity was installed, accounting for 46.7% of the total installed capacity [8].

Traditionally, solar cell technologies are divided into three generations [9]:

1.1.1 First Generation

First generation solar cells are mainly based on silicon wafers. Typically, these cells show about 15-20 % conversion efficiency. These types of solar cells dominate the market and are mostly those seen on rooftops. The major benefits of this solar cell technology are their good performance and high stability. However, they are rigid (i.e. they cannot be used for the cases where flexibility is necessary) and require a lot of energy in production (since their processability depend on vacuum deposition methods).

1.1.2 Second Generation

The second generation solar cells are based on amorphous silicon, CIGS and CdTe which typically demonstrate a performance of about 10 - 15%. It has been possible to reduce production costs of these types of solar cells compared to the first generation, since this solar cell technology avoid the use of silicon wafers and have a lower material consumption,. The second generation solar cells can also show flexibility property to some degree. However, there is still a large energy consumption associated with the production of these solar cells, since their production still include vacuum processes and high temperature treatments. Furthermore, these cells are based on scarce elements which are a limiting factor in the price.

1.1.3 Third Generation

Organic solar cells (OSCs) are regarded as third generation solar cells. These cells use organic materials, such as, small molecules or polymers. Thus, polymer solar cells can be considered as a sub category of organic solar cells. However, in general, these two terms – ‘polymer solar cell’ and ‘organic solar cell’ are used interchangeably in literature. The third generation also covers expensive

high performance experimental multi-junction solar cells which hold the world record in solar cell performance. However, because of the very high production price, this type of cells has little commercial application. On the other hand, organic solar cells offer several advantages, such as, simple, quick and inexpensive large-scale production and the use of materials that are readily available and potentially inexpensive. These solar cells can be fabricated with well-known industrial roll-to-roll (R2R) technologies that can be compared to the printing of newspapers. Although the performance and stability of organic materials based third generation solar cells is still limited compared to first and second generation solar cells, they have great potential in solar cell technology [9].

1.2 Basics of Photovoltaic Energy Conversion

The collection of light-generated carriers does not by itself give rise to power generation. In order to generate power, a voltage must be generated as well as a current. Voltage is generated in a solar cell by a process known as the "photovoltaic effect" as shown in Fig. 1.1. The collection of light-generated carriers by the p-n junction causes a movement of electrons to the n-type side and holes to the p-type side of the junction. Under short circuit conditions, there is no build up of charge, as the carriers exit the device as light-generated current [10,11].

However, if the light-generated carriers are prevented from leaving the solar cell, then the collection of light-generated carriers causes an increase in the number of electrons on the n-type side of the p-n junction and a similar increase in holes in the p-type material. This separation of charge creates an electric field at the junction, which is in opposition to that already existing at the junction, thereby reducing the net electric field.

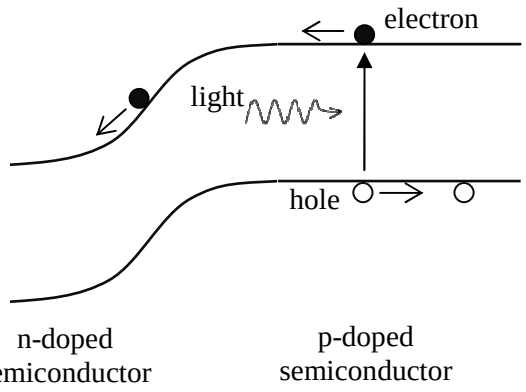

Fig. 1.1. Band diagram of a p-n junction silicon solar cell.

Since the electric field represents a barrier to the flow of the forward bias diffusion current, the reduction of the electric field increases the diffusion current. A new equilibrium is reached in which a voltage exists across the p-n junction. The current from the solar cell is the difference between light generated current (I_L) and the forward bias current.

Under open circuit conditions, the forward bias of the junction increases to a point where the light-generated current is exactly balanced by the forward bias diffusion current, and the net current is zero. The voltage required to cause these two currents to balance is called the "open-circuit voltage".

In equilibrium (i.e. in the dark) both the diffusion and drift current are small. Under short circuit conditions, the minority carrier concentration on either side of the junction is increased and the drift current, which depends on the number of minority carriers, is also increased. Under open circuit conditions, the light-generated carriers forward bias the junction, thus increasing the diffusion current. Since the drift and diffusion current are in opposite direction, there is no net current from the solar cell at open circuit [12,13].

1.3 The Organic Solar Cell

1.3.1 Potential Advantages of Organic Solar Cells

Organic solar cells (OSCs) have got numerous potential advantages including flexibility, processability and low material cost. The flexibility feature allows these solar cells to be incorporated into applications where flexibility is an advantage and/or necessity. One interesting example would be the solar panels that can be rolled out onto a roof or other surfaces. Another major selling point of organic solar cell is its Processability. Both first and second generation solar cells depend on vacuum deposition methods which require massive amounts of energy. On the other hand, for polymer based organic solar cells, layers are processed from solution and, thereby, complete solution processed cells get a possibility [14]. This unique characteristic allows for up-scaling the production which reduces the cost per area of organic solar cells considerably. It is possible to use large rolls of substrate where layers are deposited using printing or coating techniques. In general, this method is referred to as roll-to-roll coating. Using organic solar cells, the aspect of low material cost and minimal use of scarce materials can be realized. There are many second generation solar cells which utilize materials that are scarce in nature. With organic solar cells this problem can be avoided [15,16,17].

1.3.2 Operation of Organic Solar Cells: A Brief Overview

Like all solar cells, the organic solar cell converts light into electricity, by converting a flux of photons (light) into a flux of charged particles (a current). This conversion process is made possible by the combination of several types of materials, all having distinct electrical and optical characteristics [18,19,20]. Among the major two types of OSC (bilayer and bulk heterojunction (BHJ) structure) configurations – BHJ structure (Fig. 1.2) has got extensive attention for its comparative high power conversion efficiency [21-24]. Recently, a research group has also reported an internal

quantum efficiency (fraction of collected carriers per absorbed photon) close enough to 100% for BHJ structure [24], which is an indication of its potentiality to achieve high device efficiency.

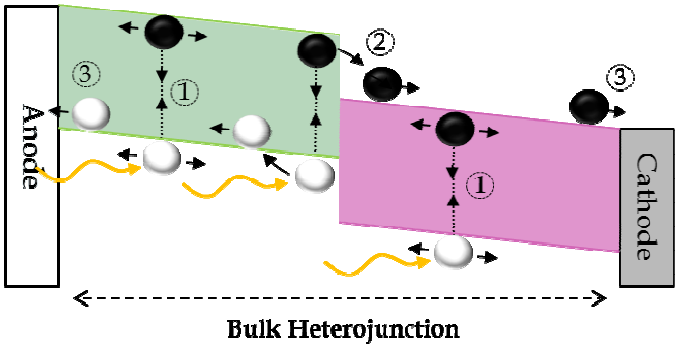

Fig. 1.2. The working principle of the organic solar cell. Light enters the cell through the transparent anode, and is absorbed in the bulk heterojunction layer through generation of excitons (1). The excitons diffuse in the bulk heterojunction until they either recombine or reach a donor-acceptor interface, where they separate into electrons (black) and holes (white) (2). The electrons and holes will then move to the respective cathode and anode, through the donor and acceptor material phase (3).

In BHJ configuration, a photoactive layer is formed by mixing an electron donating material (typically conjugated polymer) with an electron accepting material (such as, fullerene or fullerene derivatives) [23,25]. Excitons (tightly bound electron-hole pair) are generated when this active layer is exposed to photons with sufficient energy [Fig. 1.2 (step 1)]. The excitons diffuse in the bulk heterojunction until they either recombine or reach a donor-acceptor (D-A) interface, where they separate into electrons (black) and holes (white) [Fig. 1.2 (step 2)]. The electrons and holes will then move to the respective cathode and anode, through the donor and acceptor material phase [Fig. 1.2 (step 3)] [23, 26]. Due to the high number of D-A interfaces, an exceptionally high internal quantum efficiency can be achieved in this configuration. It is considered to be the most promising candidate for OSC [23, 24]. Conversely, excitons decay to the ground states before reaching to the D-A interface in bilayer configuration (where a single D-A interface exists) due to the small diffusion length of excitons (~ 10 nm) [23].

1.3.3 Some Basic Concepts Related to Light Absorption and Carrier Generation

a) Absorption of Light

Photons incident on the surface of a semiconductor will be either reflected from the top surface, will be absorbed in the material or, failing either of the above two processes, will be transmitted through the material [12].

When the energy of a photon is equal to or greater than the band gap of the material, the photon is absorbed by the material and excites an electron into the conduction band. The generation of charge carriers by photons is the basis of the photovoltaic production of energy.

b) Absorption Coefficient

The absorption coefficient determines how far into a material light of a particular wavelength can penetrate before it is absorbed [12]. Different semiconductor materials have different absorption coefficients. Materials with higher absorption coefficients more readily absorb photons, which excite electrons into the conduction band. Knowing the absorption coefficients of materials aids engineers in determining which material to use in their solar cell designs.

c) Air Mass

The Air Mass is the path length which light takes through the atmosphere normalized to the shortest possible path length (that is, when the sun is directly overhead). The Air Mass quantifies the reduction in the power of light as it passes through the atmosphere and is absorbed by air and dust [12].

In other words, the air mass represents the proportion of atmosphere that the light must pass through before striking the Earth relative to its overhead path length, and is equal to Y/X as shown in Fig. 1.3.

The Air Mass is defined as:

$$AM = \frac{1}{\cos\theta} \tag{1.1}$$

where, θ is the angle from the vertical (zenith angle). When the sun is directly overhead, the Air Mass is 1.

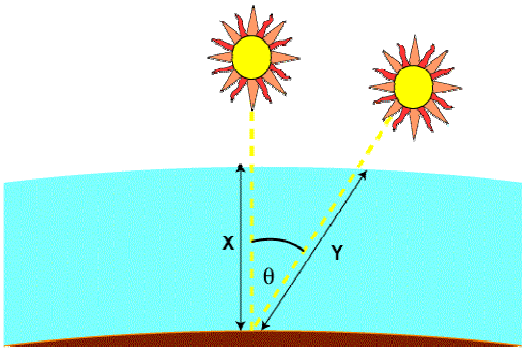

Fig. 1.3. Air Mass [12].

A comparison of solar radiation outside the Earth's atmosphere with the amount of solar radiation reaching the Earth itself is shown in Fig. 1.4.

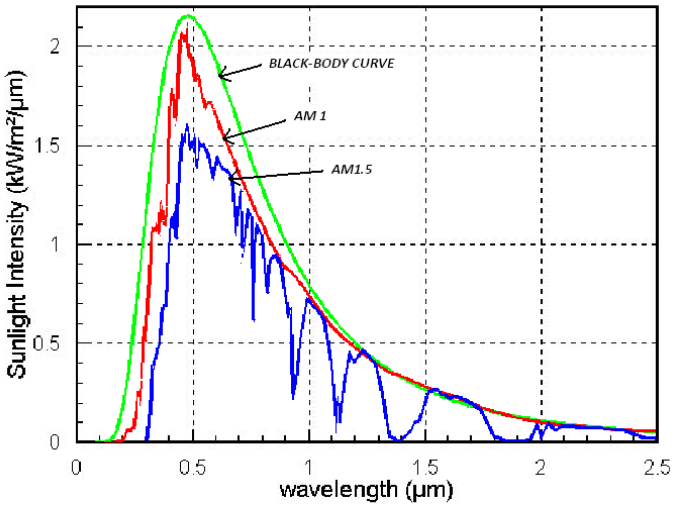

Fig. 1.4. Sunlight intensity for different air mass [12].

d) Light Absorption and Carrier Generation in OSC

Traditionally, the Beer–Lambert law is often used to describe the light intensity in bulk materials, assuming an exponential decay as [12]

$$I(x) = I_0 \exp(-\alpha x) \tag{1.2}$$

where $I(x)$ is the light intensity at position x, I_0 is the incident light intensity, and α is the absorption coefficient. However, light absorption in organic solar cells is greatly affected by optical interference given that the thickness of each layer is less than the light wavelength.

Since the thickness of thin films in organic solar cells is generally less than the wavelength of incident light, the optical effects, such as, reflections and interference are important and cannot be neglected when evaluating the electromagnetic field inside the device. The behavior of the light in the devices or the electromagnetic field distribution can be calculated either from optical transfer matrix or from Maxwell equations. In this work, optical transfer matrix formalism (TMF) has been used.

Optical transfer matrix theory is an approach to model the light propagation through a 1-D layered stack of different materials. To apply optical transfer-matrix theory in simulation of optical absorption and light intensity distribution within an organic thin-film solar cell, several assumptions need to be made [23].

1) Layers included in the device are considered to be homogeneous and isotropic.

2) Interfaces are parallel and flat compared with the wavelength of the light.

3) The light incident at the device can be described by plane waves.

Optical transfer matrix method is usually considered as an elegant approach for thin film based multilayer structures. Using this method, we can successfully calculate the optical electric field and the transmittance, reflectance and absorbance in each layer of a multilayer stack [23]. Within the transfer matrix formalism light is considered as a plane wave and perpendicular to the surface of the device. The interfaces of the multilayer stack are assumed to be parallel and the stack is described by a product of interface and layer matrices which is known as system transfer matrix [23]. In this work, we have used the carrier generation rate expression derived from optical transfer matrix method [23, 28], which will be discussed in the next chapter.

e) Electron-Hole Pair Dissociation in BHJ OSC

Excitons (bound electron-hole pair) are generated due to the light absorption. These excitons are tightly bounded because of the low dielectric constant of organic materials [26]. However, due to the presence of sufficient D-A interfaces in BHJ structure, excitons can easily reach to them and dissociate into bound electron-hole (e-h) pairs (electron and hole are in the acceptor and donor materials, respectively) [23, 26] as already mentioned in section 1.3.2. These bound e-h pairs can either recombine or can be dissociated into free electrons and holes. This dissociation process is

strongly electric field and temperature dependent [26]. Further discussions about this issue are given in subsequent chapters.

1.4 Literature Review

Although 10.6% efficiency has been achieved recently for tandem organic BHJ solar cells [23], further optimization and engineering of this structure may raise the efficiency beyond this limit [23, 24]. Therefore, accurate and efficient device models of BHJ configuration are required to optimize its performance and to utilize its exceptionally high internal quantum efficiency to its full extent. The modeling of organic BHJ solar cells has been extensively investigated [25-28]. However, most of them are limited to numerical studies or models. Few research groups [29-31] have also performed analytical modeling of the current-voltage (*J-V*) characteristic of BHJ OSCs. Marsh *et al.* [29] proposed a physically based analytical model of *J-V* curve under illumination. However, since they ignored the drift and diffusion charge transport, their model cannot predict both dark currents and illuminated characteristics at the open circuit voltage region [31]. Kumar *et al.* [30] derived their model on the basis of empirical fitting parameters (by drawing an analogy with classical p-n junction models) without considering the carrier generation and recombination processes physically.

More practical and physically-based analytical model for BHJ OSCs has been proposed by Altazin *et al.* [31]. However, they have assumed constant carrier generation rate throughout the device structure to keep the equations simple to obtain an analytical model. This approximation could lead to a deviated *J-V* characteristic from numerical studies and eventually may predict a less accurate device efficiency. This issue has been discussed in our results and discussion section. A more accurate model can be obtained considering the position dependence (i.e. spatial distribution) of the generation rate function, since the magnitude of carrier generation rate shows space dependency [25, 27]. Most of the models incorporating position dependent generation rate are numerical [25, 27, 28]. These numerical

models have used optical transfer matrix formalism [32] to obtain the carrier generation rate profile. Optical effects such as reflections and interference become important due to the thin layers in OSC structure. Transfer matrix method can successfully model these phenomena and eventually introduces oscillating feature (which arises from the interference effect) in the carrier generation rate profile with respect to position [23, 32]. In this context, an analytical model incorporating the position dependency of generation rate by following optical transfer matrix method becomes useful to avoid numerical complexities. However, no such model has been reported yet in the literature. In addition, a wavelength dependent photocurrent expression of this device based on transfer matrix method has also not been proposed yet. It is important to mention that Altazin *et al.* [31] has ignored the recombination of free charge carriers in their model. They have showed that the developed model is particularly useful to the scenario where carrier recombination rate is negligible compared to the generation rate. For example, Monestier *et al.* [27] found negligible recombination loss in their device sample and described their experimental data by ignoring recombination terms in the calculation. Recombination loss may vary with material purity and preparation condition. Presence of various impurities in starting materials can form recombination sites and eventually may affect the charge transport process [33]. Few recent analytical and numerical models [34-36] have incorporated first order recombination of free charge carriers avoiding proper recombination dynamics. Ignoring necessary recombination dynamics whether reasonable enough or not is required to be investigated.

Moreover, for some particular cases it may become indispensable to use the published data of carrier generation rate profile into the transport equations to derive a model, where the profile can be the outcome of experiments or complicated numerical simulations. However, all these carrier generation rate profiles are required to be represented by some sort of arithmetic expression to derive an analytical model of OSC. For these cases, a generalized empirical formula of carrier generation rate profile becomes a useful tool to derive the *J-V* characteristic expression of BHJ OSC. However, no such formula has been proposed yet in literature. It is important to mention that Furlan and Amon

[13] proposed an empirical expression of generation rate for traditional solar cells (where generation rate experiences exponential decay with respect to position) to improve the computational efficiency. However, this expression cannot be applied to the thin film based structures (because of the oscillating nature of carrier generation profile).

1.5 Objectives of the Thesis

The objectives of this thesis are:

i. To develop an optoelectronic analytical model of current-voltage characteristics for BHJ organic solar cells.

ii. To incorporate spatial distribution of photocarrier generation rate in the model using transfer matrix formalism unlike previous analytical models.

iii. To include e-h pair dissociation probability in the model and study the effect of this probability on device performance.

iv. To propose an empirical expression of space dependent photocarrier generation rate (for the cases where the generation rate profile cannot be expressed in a physics-based closed form expression).

v. To develop an analytical model using the proposed empirical generation rate.

vi. To compare the results of the derived models with numerical simulations and published experimental data.

vii. To compare the performance of the developed analytical models with previous analytical models in predicting experimental and numerical simulation results.

1.6 Thesis Overview

This thesis is divided into four chapters.

Chapter 1 provides general introduction followed by the background, literature review and the objectives of the work.

Chapter 2 covers the mathematical analysis to develop the novel BHJ OSC model using transfer matrix formalism (described in section 2.1). Additionally, in this chapter, a new empirical expression of carrier generation rate profile is proposed and incorporated in the carrier transport equations to develop another BHJ OSC model (described in section 2.2).

The results obtained from the derived models (one model derived using transfer matrix formalism and the other one derived using empirical expression of carrier generation rate profile) are discussed in chapter 3. Verifications of the derived models with experimental and numerical results are discussed in this chapter. Furthermore, effect of different model parameters on the device performance are also mentioned in this chapter.

Chapter 4 contains the concluding remarks along with suggestions for future work on the topic.

Chapter 2

Device Modeling[1]

This chapter provides detail derivations of the BHJ OSC models. The OSC model derivation using the carrier generation rate profile obtained from the optical transfer matrix formalism (TMF) is described in section 2.1. And, the OSC model derivation using the empirical expression of carrier generation rate profile is given in section 2.2.

2.1 Analytical Model of BHJ OSC Device Considering Spatial Distribution of Carrier Generation Obtained from TMF

We have considered a typical BHJ OSC structure as shown in Fig. 2.1(a) (not in scale) in this study. The dimensions of different layers (Fig. 2.1(a)) are similar to the structure studied by Monestier *et al.* [27]. The active layer of this OSC is a poly(3-hexylthiophene):[6,6]-phenyl-C_{61}-butyric acid methyl ester (P3HT:PCBM) blend (1:1 by weight ratio) which is sandwiched between 100 nm aluminum layer (cathode) and 45 nm thick poly(3,4–ethylenedioxythiophene):poly(styrenesulfonate) (PEDOT:PSS) layer. A 180 nm thick indium tin oxide (ITO) layer (anode) covers the PEDOT:PSS film. The active layer thickness has been varied to analyze our derived expression. We have used the terms active layer thickness and blend thickness interchangeably throughout the paper. Figure 2.1(b) shows a schematic energy level diagram of different device layers (before the materials are brought into contact). The potential energy values mentioned in Fig. 2.1(b) are commonly used in literature [23, 25, 37, 38]. We have considered PEDOT:PSS as the injecting layer [25, 30, 31]. When the device

[1] A version of this chapter has been published in a peer-reviewed journal (Reused with permission from "M.M. Chowdhury, M.K. Alam, 'An optoelectronic analytical model for bulk heterojunction organic solar cells incorporating position and wavelength dependent carrier generation', *Solar Energy Materials and Solar Cells*, vol. 132, pp. 107-117, 2015", Copyright 2014, *Elsevier*).

is exposed to sunlight (or other light sources) the incident photons with sufficient energy are absorbed in the active layers and excitons are generated. These excitons are tightly bounded because of the low dielectric constant of organic materials [36]. However, due to the presence of sufficient D-A interfaces in BHJ structure, excitons can easily reach to them and dissociate into bound electron-hole (e-h) pairs (now electron and hole are in the acceptor and donor materials, respectively) [23, 26]. The dissociation process is driven by the difference in LUMO (lowest unoccupied molecular orbital) levels of donor and acceptor materials (The process is assumed to be a field independent phenomenon having a quantum efficiency of almost unity [26]). These bound e-h pairs can either recombine or can be separated into free electrons and holes. Subsequently, the free carriers in the active layer are diffused and drifted to the corresponding electrodes as shown in Fig. 2.1(a) [23, 26, 31]. The active layer (P3HT:PCBM blend) has been modeled by a single meta-material consists of HOMO (highest occupied molecular orbital) of the donor material and LUMO of the acceptor material (similar to the valence and conduction band, respectively) [26, 27, 30, 31].

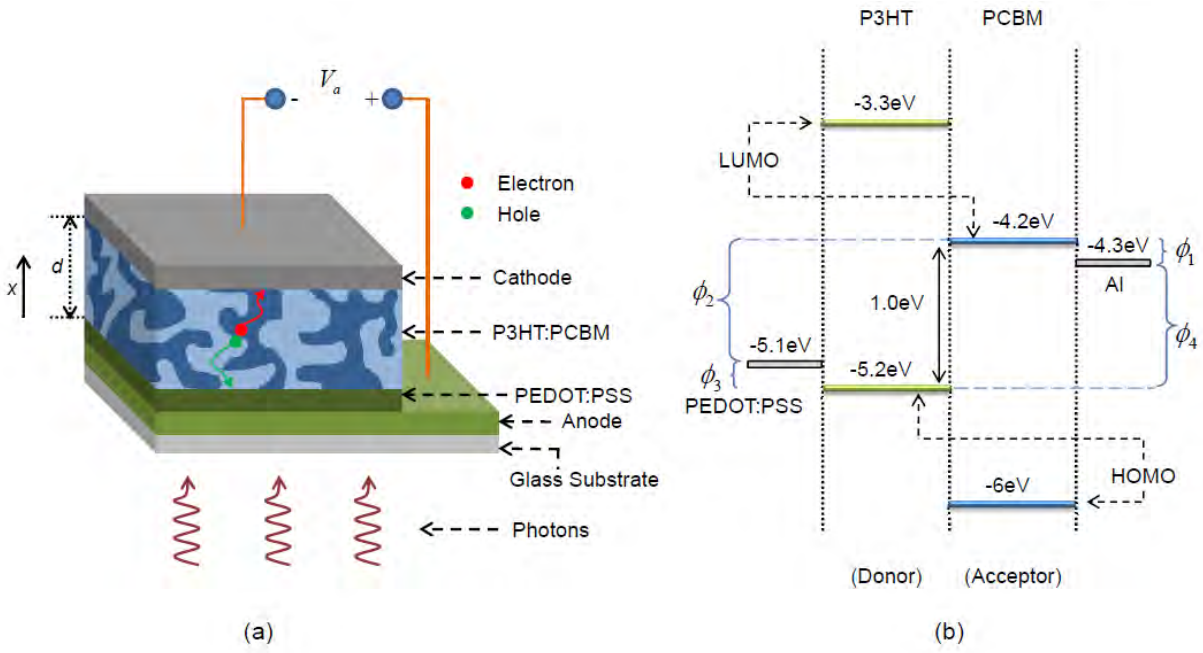

Fig. 2.1. (a) Configuration of P3HT:PCBM based BHJ OSC and (b) Schematic energy potential diagram of the considered cell (before the materials are brought into contact).

In this section, we present the expression of OSC *J-V* characteristic under illuminated conditions. To derive the expression we have utilized current density and continuity equations of classical semiconductor devices [39, 40], which have been extensively used to describe the electrical behavior of OSC as well [26, 27, 31].

2.1.1 Drift-Diffusion Equations

The current density equations can be written as:

$$J_p = q\mu_p pE - qD_p \frac{dp}{dx}, \tag{2.1}$$

$$J_n = q\mu_n nE + qD_n \frac{dn}{dx}, \tag{2.2}$$

where $J_{p(n)}$ is the hole (electron) current density, q is the unit charge, p and n are hole and electron density, $\mu_{p(n)}$, $D_{p(n)}$ are the hole (electron) mobility, hole (electron) diffusion coefficient, respectively and E is the electric field within the active layer of the device structure. Classical Einstein relation ($D_{p(n)} / \mu_{p(n)} = kT / q = V_T$) has been used for the diffusion coefficients, where k is the Boltzmann's constant, T is the absolute temperature and V_T is the thermal voltage. Although diffusion coefficient may not obey the Einstein's relation exactly for disordered materials, researchers have been using this relation for simplicity without experiencing any notable deviation [25-28, 30, 31]. We consider only one spatial dimension (along the thickness of the active layer) for the equations, since the thickness (typically in nm range) to lateral dimensions (typically in mm range) ratio is too small [26]. The free charge carriers are diffused and drifted in the active layer according to the Eqs. (2.1) and (2.2). The electric field E within the active layer assists the carrier drift process.

It is important to mention that similar to the inorganic amorphous semiconductors, disorder in a BHJ system introduces localized band tail states in the electronic structure [41, 42]. These band tails are used to explain different electronic transport phenomena in disordered systems. It is considered that the charge density dependence of mobility is associated to the band tails [43]. In addition, these tail states are also used to explain temperature and electric field dependent charge carrier mobility in disordered systems [42]. However, occurrences of these phenomena are related to various factors. For example, it has been reported that depending on polymer molecular weight and morphology, P3HT may show relatively weak relation of carrier mobility with electric field and temperature [43, 44], which ultimately influences the P3HT:PCBM blend carrier mobility (as well as its dependency on electric field) also [44]. Therefore, the extent of the aforementioned phenomena may vary from materials to materials, their film preparation conditions and morphologies. Moreover, it has been found that the carrier mobility dependence on electric field and carrier concentration can be considered weak at low electric field and low carrier concentration, and a constant mobility may be assumed from short-circuit to open-circuit range [23]. As a result, many research groups [23, 25-27, 30, 31, 36, 45] have ignored these phenomena (e.g. dependency of mobility on charge density, electric field and temperature) in their BHJ OSC models for simplicity without experiencing significant deviation from experimental results. In the present work, the disorder-induced band tail states and their corresponding effects have also been considered negligible following the previous models.

2.1.2 Calculation of Electric Field

Since the typical active layer thickness of BHJ OSC is in nanometer range (generally 70 nm to 150 nm), the electric field (E) within this layer can be approximated by a constant quantity [27, 29-31]. This uniform electric field approximation allows us to develop a complete analytical expression of the *J-V* characteristics. Same assumption has also been used in previous analytical models [29-31] as well

as in numerical simulation [27] for such devices. Under the uniform electric-field approximation, the electrostatic field can be written as [27, 29-31]:

$$E = \frac{V_a - V_{bi}}{d}, \tag{2.3}$$

where d is the active layer thickness, E is the electric field through the whole active layer, V_a is the terminal voltage (note that conventionally V_a is termed as applied bias in literature), and V_{bi} is the built-in potential of the device. V_{bi} can be calculated from the difference of the electrodes work-functions [30, 31, 46]. For higher thicknesses (usually greater than 250 nm), uniform electric field approximation may no longer be valid [31]. For such cases, Poisson equation should be solved self-consistently with the Eqs. (2.1)-(2.2) [26, 31].

2.1.3 Continuity Equations

At steady state, the continuity equations are written as [26, 39]:

$$\frac{1}{q}\frac{dJ_p}{dx} = G - R_p, \tag{2.4}$$

$$-\frac{1}{q}\frac{dJ_n}{dx} = G - R_n, \tag{2.5}$$

where $R_{p(n)}$ is the recombination rate of holes (electrons) and G is the carrier generation rate.

While moving toward the electrodes the free charge carriers may recombine. The recombination mechanisms in BHJ OSC are far from clear and still a matter of debate [23, 47]. However, in general, it is considered that the free electrons and holes may undergo first order (monomolecular) and/or bimolecular recombination processes [23, 47]. In some cases, free charge carrier recombination is negligible and can be suppressed in front of generation rate (which is the case considered in this work

and discussed later in this section) [27, 31]. As mentioned earlier, some analytical and numerical models [34-36] have incorporated monomolecular recombination of free charge carriers without considering appropriate dynamics and have used different recombination terms for both free carriers in steady state. Therefore, these models do not yield a constant current density throughout the device structure, although they can match experimental results with the help of fitting parameters. When the Eqs. (2.4) and (2.5) are to be used for BHJ structure (in steady state), proper recombination dynamics [47] should be taken into consideration since we are unable to apply minority carrier approximations in this case [48]. Therefore, we have not incorporated the recombination phenomena following these models and our model is applicable to the samples where recombination can be ignored. It can also be noted that the transport equations become intractable to solve analytically (for both monomolecular and bimolecular recombination cases) if we attempt to use appropriate dynamics [47] for recombination phenomena.

2.1.4 Differential Equations of Carrier Density Profiles

Using Eqs. (2.1) and (2.2) in Eqs. (2.4) and (2.5), respectively and assuming electric field as a constant quantity, the continuity equations can be written in the following form:

$$-V_T \mu_p \frac{d^2 p}{dx^2} + E \mu_p \frac{dp}{dx} = G\left(x, \lambda\right), \tag{2.6}$$

$$-V_T \mu_n \frac{d^2 n}{dx^2} - E \mu_n \frac{dn}{dx} = G\left(x, \lambda\right), \tag{2.7}$$

The recombination terms have been ignored in Eqs. (2.6) and (2.7) assuming that the terms are negligible. Same approximation has been previously used by other authors [27, 31]. From rigorous numerical simulation, Altazin *et al.* [31] found that this approximation is valid when electrons and holes have mobility values not differing by more than a factor (μ_n / μ_p) of ~50. Otherwise, charges tend to accumulate inside the active layer due to the large difference in the transport properties and

eventually space charge is formed and recombination is enhanced as well [31, 49, 50]. Moreover, due to the space charge effect, uniform electric field approximation [Eq. (2.3)] may become invalid and Poisson equation may need to be solved self-consistently with the transport equations. However, in our present study, the factor μ_n / μ_p is within ~15 (we have taken the mobility values from Ref. [27], since experimental data used in the present work have also been extracted from this reference). Therefore, the space charge effect and the recombination of free charge carriers have been ignored in this work. These phenomena cannot be neglected if the charge transport becomes considerably unbalanced (for both increasing or decreasing value of μ_n / μ_p) in a BHJ sample [31, 50]. Since analytical solution of the transport equations become intractable for these cases, numerical model and simulations will be required.

It is noteworthy that we have expressed the carrier generation term (G) as a function of position, x and incident wavelength, λ in the above equations [(2.6) and (2.7)]. When the carrier generation rate is not constant (rather a function of position, x), the differential equations in (2.6) and (2.7) become difficult to solve analytically. To keep the equations simple Altazin *et al.* [31] replaced the generation rate, $G(x) = \int_{\lambda_1}^{\lambda_2} G(x,\lambda) d\lambda$ by an averaged carrier generation rate G_{avg}, given as

$$G_{avg} = \frac{1}{d} \int_0^d G(x)\, dx, \tag{2.8}$$

However, to make our model more realistic, we have explicitly considered the position and wavelength dependent generation rate obtained from optical transfer matrix method [32]. Since the thickness of thin films in OSC are usually less than the wavelength of the incident light, reflections and interference effects become important unlike the conventional structure consists of bulk materials (generally in μm range). Traditionally, it is assumed that light intensity experiences exponential decay in the propagating direction inside the bulk materials (known as Beer-Lambert law) [23]. However, it

cannot explain the light intensity in thin films because of the considerable reflections and interferences in different layers [23, 28, 32]. Therefore, optical transfer matrix method is usually considered as an elegant approach for thin film based multilayer structures (Fig. 2.1(a)). Using this method, we can successfully calculate the optical electric field and the transmittance, reflectance and absorbance in each layer of a multilayer stack similar to the structure we described in Fig 2.1(a) [32]. Within the transfer matrix formalism light is considered as a plane wave and perpendicular to the surface of the device. The interfaces of the multilayer stack are assumed to be parallel and the stack is described by a product of interface and layer matrices which is known as system transfer matrix [23, 32]. We have used the carrier generation rate expression derived from optical transfer matrix method [23, 28, 32]. The generation rate as a function of wavelength and position can be written as:

$$G(x,\lambda)=\frac{\lambda}{hc}\alpha_j T_j I_0(\lambda)\begin{bmatrix}\exp(-\alpha_j x)+\rho_j^{"2}\exp(-\alpha_j(2d-x))\\ +2\rho_j^{"}\exp(-\alpha_j d)\cos\left(\frac{4\pi n_j}{\lambda}(d-x)+\delta_j^{"}\right)\end{bmatrix}, \tag{2.9}$$

where $I_0(\lambda)$ is the intensity of the incident light with standard AM 1.5 distribution, $\rho_j^{"}$ and $\delta_j^{"}$ are the absolute value and the argument of the complex reflection coefficient, respectively and $T_j=(n_j/n_0)\left|t_j^{+}\right|^2$ is the internal intensity transmittance (n_j and n_0 are the refractive indices of active layer and ambient, respectively, t_j^{+} is an internal transfer coefficient [expression has been given below]); λ, α_j, d, h and c are wavelength of the incident photon, absorption coefficient of the active layer, thickness of the active layer, Planck's constant and light speed in a vacuum, respectively. The subscript j refers to the active layer. Detail descriptions as well as the expressions of these parameters and optical constants of material used in this study can be found in Ref. [23]. Any modification in the layer thicknesses of the stack is modeled by transfer matrix method and the corresponding effect in the carrier generation rate is described by Eq. (2.9). Detail explanation of the method as well as the derivation of Eq. (2.9) is available in the work of Pettersson *et al*. [32]. In short, the first and second

terms inside the square bracket of $G(x)$ expression (Eq. 2.9) arise from the optical electric field propagating in the positive and negative x directions, respectively. These two fields interfere with each other and originate the third term which introduces the oscillating feature in the carrier generation rate profile with respect to position x. When the layer thickness (d) is less than the wavelength of incident light, the third term becomes significantly important [23].

The internal transfer coefficient t_j^+ is defined as follows [23,28,32]

$$t_j^+ = \left[S'_{j11} + S'_{j12} r''_j \exp\left(2ik_j d_j\right) \right]^{-1}$$

where,

$$r''_j = S'_{j21} / S'_{j11}$$

and

$$S'_j = \begin{bmatrix} S'_{j11} & S'_{j12} \\ S'_{j21} & S'_{j22} \end{bmatrix} = \left(\prod_{v=1}^{j-1} I_{(v-1)v} L_v \right) I_{(j-1)j}$$

$$S''_j = \begin{bmatrix} S''_{j11} & S''_{j12} \\ S''_{j21} & S''_{j22} \end{bmatrix} = \left(\prod_{v=j+1}^{m} I_{(v-1)v} L_v \right) I_{m(m+1)}$$

where, the interface matrix I_{jk}, for the interface between j and $k = j+1$ layers, is expressed as

$$I_{jk} = \begin{bmatrix} \left(\tilde{n}_j + \tilde{n}_k\right)/2\tilde{n}_j & \left(\tilde{n}_j - \tilde{n}_k\right)/2\tilde{n}_j \\ \left(\tilde{n}_j - \tilde{n}_k\right)/2\tilde{n}_j & \left(\tilde{n}_j + \tilde{n}_k\right)/2\tilde{n}_j \end{bmatrix}$$

and, the layer matrix L_j is described as

$$L_j = \begin{bmatrix} \exp\left(-i\frac{2\pi\tilde{n}_j}{\lambda}d_j\right) & 0 \\ 0 & \exp\left(i\frac{2\pi\tilde{n}_j}{\lambda}d_j\right) \end{bmatrix}$$

where, $\tilde{n}_j$ is the complex index of refraction, and defined as $\tilde{n}_j = n_j + i\kappa_j$. Here, n_j and κ_j are the real (refractive index) and imaginary (extinction coefficient, $\kappa_j = \alpha_j\lambda/(4\pi)$) parts of the complex refractive index $\tilde{n}_j$.

2.1.5 Solutions of the Carrier Density Profiles

Using Eq. (2.9) in Eqs. (2.6) and (2.7), the solution for carrier density can be written in the following forms, respectively:

$$p(x) = \left[A_{1,dark} + A_{2,dark}\exp\left(\frac{E}{V_T}x\right)\right]_{dark} + \int_{\lambda_1}^{\lambda_2}\left[A_{1,ph} + A_{2,ph}\exp\left(\frac{E}{V_T}x\right) + f_p(x,\lambda)\right]_{ph} d\lambda, \tag{2.10}$$

$$n(x) = \left[B_{1,dark} + B_{2,dark}\exp\left(-\frac{E}{V_T}x\right)\right]_{dark} + \int_{\lambda_1}^{\lambda_2}\left[B_{1,ph} + B_{2,ph}\exp\left(-\frac{E}{V_T}x\right) + f_n(x,\lambda)\right]_{ph} d\lambda, \tag{2.11}$$

where

$$f_p(x,\lambda) = -\frac{K(\lambda)}{\mu_p V_T}\left[\frac{\exp(-\alpha_j x)}{\alpha_j^2 + \frac{E}{V_T}\alpha_j} + \frac{\rho_j^{"2}\exp(-2\alpha_j d + \alpha_j x)}{\alpha_j^2 - \frac{E}{V_T}\alpha_j} - M(\lambda)\left[g(x,\lambda) - h(x,\lambda)\right]\right], \tag{2.12}$$

$$f_n(x,\lambda) = -\frac{K(\lambda)}{\mu_n V_T}\left[\frac{\exp(-\alpha_j x)}{\alpha_j^2 - \frac{E}{V_T}\alpha_j} + \frac{\rho_j^{"2}\exp(-2\alpha_j d + \alpha_j x)}{\alpha_j^2 + \frac{E}{V_T}\alpha_j} - M(\lambda)\left[g(x,\lambda) + h(x,\lambda)\right]\right], \tag{2.13}$$

$$g(x,\lambda) = \frac{\cos\left(-\frac{4\pi n_j}{\lambda}x + \frac{4\pi n_j}{\lambda}d + \delta_j^{"}\right)}{\left(\frac{4\pi n_j}{\lambda}\right)^2 + \left(\frac{E}{V_T}\right)^2}, \tag{2.14}$$

$$h(x,\lambda) = \frac{\frac{E}{V_T}\sin\left(-\frac{4\pi n_j}{\lambda}x + \frac{4\pi n_j}{\lambda}d + \delta_j^{"}\right)}{\left(\frac{4\pi n_j}{\lambda}\right)^3 + \left(\frac{E}{V_T}\right)^2\left(\frac{4\pi n_j}{\lambda}\right)}, \tag{2.15}$$

$$K(\lambda) = \frac{\lambda}{hc}\alpha_j(\lambda)T_j I_0(\lambda), \tag{2.16}$$

$$M(\lambda) = 2\rho_j^{"}\exp\left[-\alpha_j(\lambda)d\right], \tag{2.17}$$

The constants $A_{1,dark(ph)}$, $A_{2,dark(ph)}$, $B_{1,dark(ph)}$ and $B_{2,dark(ph)}$ can be determined using the boundary conditions [30, 39]:

$$p(0) = N_V\exp\left(-\frac{\phi_3}{V_T}\right),\ p(d) = N_V\exp\left(-\frac{\phi_4}{V_T}\right),\ n(0) = N_C\exp\left(-\frac{\phi_2}{V_T}\right) \text{ and } n(d) = N_C\exp\left(-\frac{\phi_1}{V_T}\right)$$

ϕ_1, ϕ_2, ϕ_3 and ϕ_4 are defined in Fig. 2.1(b).

The expressions for $A_{1,dark(ph)}$, $A_{2,dark(ph)}$, $B_{1,dark(ph)}$ and $B_{2,dark(ph)}$ (after applying the boundary conditions) are obtained as follows:

$$A_{1,dark} = \frac{N_V\left(\exp\left(-\frac{\phi_4}{V_T}\right)-\exp\left(\frac{-\phi_3+Ed}{V_T}\right)\right)}{1-\exp\left(\frac{E}{V_T}d\right)}, A_{1,ph} = \frac{f_p(0,\lambda)\exp\left(\frac{E}{V_T}d\right)-f_p(d,\lambda)}{1-\exp\left(\frac{E}{V_T}d\right)}, \quad (2.18)$$

$$A_{2,dark} = \frac{N_V\left(\exp\left(-\frac{\phi_3}{V_T}\right)-\exp\left(-\frac{\phi_4}{V_T}\right)\right)}{1-\exp\left(\frac{E}{V_T}d\right)}, A_{2,ph} = \frac{-f_p(0,\lambda)+f_p(d,\lambda)}{1-\exp\left(\frac{E}{V_T}d\right)}, \quad (2.19)$$

$$B_{1,dark} = \frac{N_C\left(\exp\left(-\frac{\phi_1}{V_T}\right)-\exp\left(\frac{-\phi_2-Ed}{V_T}\right)\right)}{1-\exp\left(-\frac{E}{V_T}d\right)}, B_{1,ph} = \frac{f_n(0,\lambda)\exp\left(-\frac{E}{V_T}d\right)-f_n(d,\lambda)}{1-\exp\left(-\frac{E}{V_T}d\right)}, \quad (2.20)$$

$$B_{2,dark} = \frac{N_C\left(\exp\left(-\frac{\phi_2}{V_T}\right)-\exp\left(-\frac{\phi_1}{V_T}\right)\right)}{1-\exp\left(-\frac{E}{V_T}d\right)}, B_{2,ph} = \frac{-f_n(0,\lambda)+f_n(d,\lambda)}{1-\exp\left(-\frac{E}{V_T}d\right)}, \quad (2.21)$$

Using Eqs. (2.10) and (2.11), the total current density (J) can be calculated from the summation of Eqs. (2.1) and (2.2):

$$J = \left(J_{p,dark}+J_{n,dark}\right)+\int_{\lambda_1}^{\lambda_2}\left(J_{p,ph}+J_{n,ph}\right)d\lambda, \quad (2.22)$$

where the dark and photocurrent components of Eqs. (2.1) and (2.2) have been separated and represented by $J_{p,dark}$, $J_{n,dark}$ and $J_{p,ph}$, $J_{n,ph}$ respectively. Integral term on the right side of Eq. (2.22) is our photocurrent expression and the other term in bracket refers to the dark current.

2.1.6 Inclusion of e-h Pair Dissociation Probability in the Model

So far, we have considered that the rate of exciton generation equals to the free charge carrier generation rate similar to the previous works [27, 36]. However, the e-h pair generated after the dissociation process (due to the difference in LUMO levels as described earlier) is meta-stable. The pair can either decay to the ground state or can be dissociated into free carriers. This dissociation process is strongly electric field and temperature dependent [26]. We can include the effect of e-h pair dissociation probability in our model by rewriting the Eqs. (2.6) and (2.7) as follows:

$$-V_T \mu_p \frac{d^2 p}{dx^2} + E\mu_p \frac{dp}{dx} = P(E)G(x,\lambda), \tag{2.23}$$

$$-V_T \mu_n \frac{d^2 n}{dx^2} - E\mu_n \frac{dn}{dx} = P(E)G(x,\lambda), \tag{2.24}$$

where, $P(E)$ is the electric field dependent probability for an e-h pair to be dissociated into free charges following Onsager-Braun theories [51, 52]. $P(E)$ can be calculated as [26, 45]:

$$P(E) = \int_0^\infty p(a,E)\, f(a)\, da, \tag{2.25}$$

where $p(a, E)$ is e-h pair dissociation probability for a given pair distance a, $f(a)$ is a normalized distribution function. They can be calculated from the following expressions [26, 45]:

$$p(a,E) = \frac{k_{diss}(a,E)}{k_{diss}(a,E) + k_f}, \tag{2.26}$$

$$f(a) = \frac{4}{\sqrt{\pi} a_0^3} a^2 \exp\left(-\frac{a^2}{a_0^2}\right), \tag{2.27}$$

where a_0 , k_{diss} and k_f are the e-h pair average distance, dissociation rate and decay rate, respectively. The dissociation rate k_{diss} is expressed as [26, 45]:

$$k_{\text{diss}}\left(a,E\right)=\frac{3\alpha}{4\pi a^3}\exp\left(-\frac{E_b}{k_BT}\right)J_1\left(2\sqrt{-2b}\right)/\sqrt{-2b}, \tag{2.28}$$

where $\alpha=q\left(\mu_n+\mu_p\right)/\varepsilon$, J_1 is the first order Bessel function, $b=q^3\left|E\right|/\left(8\pi\varepsilon k_B^2T^2\right)$, $E_B=q^2/4\pi\varepsilon a$ is the e-h pair binding energy and ε is the dielectric constant.

It can be seen that we have integrated Eq. (2.26) over a distribution of separation distances in Eq. (2.25) using a normalized distribution function [Eq. (2.27)]. Due to the disordered characteristic of the active layer blend, it is more appropriate to consider the e-h pair distance (a) as a non-constant quantity [26]. Indeed, a distribution of distances is reasonable to be used as it has been done in Eq. (2.25) [26, 28, 45]. Considering e-h pair distance as a constant quantity may lead to significantly different result which will be discussed in the next section. To carry out the calculation considering constant e-h pair distance (a), we avoid the integration in Eq. (2.25) and replace the terms $P(E)$ in Eqs. (2.23) and (2.24) with the $p(a, E)$ expression [Eq. (2.26)] assuming that $a = a_0$. Similar approach was used in Refs. 25 and 31.

We have found that the solution of Eqs. (2.23) and (2.24) are similar to the previous case except the expression of $K(\lambda)$ in (2.16). This expression should be modified as follows:

$$K\left(\lambda\right)=P\left(E\right)\frac{\lambda}{hc}\alpha_j\left(\lambda\right)T_jI_0\left(\lambda\right), \tag{2.29}$$

The rest of the equations have the same expressions.

2.2 Analytical Model of BHJ OSC Device Using a Generalized Empirical Formula of Space Dependent Carrier Generation

In this section, we consider that we are provided with carrier generation rate profile ($G(x)$) within the active layer region. The $G(x)$ profile can be obtained from complex numerical simulations, experimental results or published data. Moreover, we assume that the given $G(x)$ profile cannot be expressed in a physics-based closed form expression unlike the TMF case as mentioned in section 2.1, and the only way to develop the OSC device model is by following an empirical expression of $G(x)$. In this situation, we have to depend on an empirical expression of $G(x)$ profile [in Eqs. (2.6) and (2.7)] to develop the device model as mentioned earlier. In this section, we will use all the physics presented in section 2.1 except the carrier generation rate profile in Eq. (2.9) (and the discussions related to it). For the carrier generation rate profile, here, we propose a new empirical expression.

It is important to mention that Furlan and Amon [13] proposed an empirical expression for traditional solar cells (usually in μm range), where they used sum of 'exponential functions' (Eq. 2.30) to model the exponential decay of carrier generation with respect to position.

$$G(x) = \sum_{i=1}^{n} a_i \exp(-b_i x) \tag{2.30}$$

where a_i, and b_i are constant terms determined by curve fitting method [13].

However, in general, due to the thin layers the carrier generation rate profile in OSC shows oscillating nature rather than the exponential decay with respect to position (as described earlier). Therefore, it is not possible to fit the generation rate profile using Eq. (2.30). However, we have found that the generation rate $G(x)$ in thin active layer can easily be approximated by a sum of sine functions as follows

$$G(x) = \sum_m a_m \sin(b_m x + c_m) \tag{2.31}$$

where a_m, b_m and c_m are constant terms. We compare this position dependent empirical expression with the data of Monestier *et al.* [27] for different active layer thicknesses and extract the values of a_m, b_m and c_m for each cases using curve fitting method (which will be described in the results and discussions section).

For the carrier generation rate profile $G(x)$ [Eq. (2.31)], we write the Eqs. (2.23) and (2.24) as follows:

$$-V_T \mu_p \frac{d^2 p}{dx^2} + E\mu_p \frac{dp}{dx} = P(E)G(x), \tag{2.32}$$

$$-V_T \mu_n \frac{d^2 n}{dx^2} - E\mu_n \frac{dn}{dx} = P(E)G(x), \tag{2.33}$$

where, $P(E)$ is the electric field dependent probability for an e-h pair to be dissociated into free charges as described in section 2.1.6.

Using the expression of $G(x)$ (from Eq. 31) in Eqs. (2.32) and (2.33) following solutions are obtained for holes and electrons, respectively

$$p(x) = A_1 + A_2 \exp\left(\frac{E}{V_T} x\right) + f_p(x), \tag{2.34}$$

$$n(x) = B_1 + B_2 \exp\left(-\frac{E}{V_T} x\right) + f_n(x), \tag{2.35}$$

where

$$f_p(x) = \frac{P(E)}{\mu_p V_T} \sum_m \frac{b_m a_m \sin(b_m x + c_m) - \frac{E}{V_T} a_m \cos(b_m x + c_m)}{b_m^3 + \left(\frac{E}{V_T}\right)^2 b_m}, \tag{2.36}$$

$$f_n(x) = \frac{P(E)}{\mu_n V_T} \sum_m \frac{b_m a_m \sin(b_m x + c_m) + \frac{E}{V_T} a_m \cos(b_m x + c_m)}{b_m^3 + \left(\frac{E}{V_T}\right)^2 b_m}, \tag{2.37}$$

The constants A_1, A_2, B_1 and B_2 can be determined using the boundary conditions [30, 39]:

$$p(0) = N_V \exp\left(-\frac{\phi_3}{V_T}\right),\ p(d) = N_V \exp\left(-\frac{\phi_4}{V_T}\right),\ n(0) = N_C \exp\left(-\frac{\phi_2}{V_T}\right) \text{ and } n(d) = N_C \exp\left(-\frac{\phi_1}{V_T}\right)$$

ϕ_1, ϕ_2, ϕ_3 and ϕ_4 are defined in Fig. 2.1(b).

The expressions for A_1, A_2, B_1 and B_2 (after applying the boundary conditions) are obtained as follows:

$$A_1 = \frac{N_V\left(\exp\left(-\frac{\phi_4}{V_T}\right) - \exp\left(\frac{-\phi_3 + Ed}{V_T}\right)\right) + f_p(0)\exp\left(\frac{E}{V_T}d\right) - f_p(d)}{1 - \exp\left(\frac{E}{V_T}d\right)}, \tag{2.38}$$

$$A_2 = \frac{N_V\left(\exp\left(-\frac{\phi_3}{V_T}\right) - \exp\left(-\frac{\phi_4}{V_T}\right)\right) - f_p(0) + f_p(d)}{1 - \exp\left(\frac{E}{V_T}d\right)}, \tag{2.39}$$

$$B_1 = \frac{N_C\left(\exp\left(-\frac{\phi_1}{V_T}\right)-\exp\left(\frac{-\phi_2 - Ed}{V_T}\right)\right)+ f_n(0)\exp\left(-\frac{E}{V_T}d\right)- f_n(d)}{1-\exp\left(-\frac{E}{V_T}d\right)}, \tag{2.40}$$

$$B_2 = \frac{N_C\left(\exp\left(-\frac{\phi_2}{V_T}\right)-\exp\left(-\frac{\phi_1}{V_T}\right)\right)- f_n(0)+ f_n(d)}{1-\exp\left(-\frac{E}{V_T}d\right)}, \tag{2.41}$$

By using the *p* and *n* solutions from Eqs. (2.34) and (2.35), the total current density can be calculated from the summation of Eqs. (2.1) and (2.2).

Chapter 3

Results and Discussions[2]

This chapter provides the results and discussions pertaining to the models derived in this thesis. The results obtained from the OSC model derived in section 2.1 using the optical transfer matrix formalism are discussed in section 3.1. And, section 3.2 discusses about the results obtained from the OSC model derived in section 2.2 using the empirical carrier generation rate expression.

3.1 Results Obtained from the TMF Based OSC Model

3.1.1 Current-Voltage Characteristics from the Derived Model and Comparison with Numerical Simulations

Figures 3.1(a) and 3.1(b) show *J-V* characteristics obtained from our analytical model (Eq. (2.22)) along with the results of previous model [31] and numerical simulation. For the numerical simulation, we have solved the Eqs. (2.6) and (2.7) with Finite Element Method using COMSOL Multiphysics [53]. Since the same equations [Eqs. (2.6) and (2.7)] have been used for numerical simulation as well as for developing the analytical model [Eqs. (2.10)-(2.22)], agreement between these two studies (numerical and analytical approaches) is obvious. Nevertheless, a comparison with the numerical simulation helps to justify the mathematical correctness of the derived expressions [e.g. Eqs. (2.10)-(2.22)]. We have studied *J-V* characteristics for two frequently used active layer thicknesses in OSC literature (100 nm and 120 nm) for the ease of comparison [26, 31, 36]. Figures 3.1(a) and 3.1(b)

[2] A version of this chapter has been published in a peer-reviewed journal (Reused with permission from "M.M. Chowdhury, M.K. Alam, 'An optoelectronic analytical model for bulk heterojunction organic solar cells incorporating position and wavelength dependent carrier generation', *Solar Energy Materials and Solar Cells*, vol. 132, pp. 107-117, 2015", Copyright 2014, *Elsevier*).

show the results for 100 nm and 120 nm thick active layers, respectively. The parameters used in this study (Table 3.1) have been taken from literature [27, 36]. Effective bandgap (E_g) in Table 3.1 is defined by the difference between acceptor LUMO level and donor HOMO level [36] (Fig. 2.1(b)). Firstly, we have considered that the rate of exciton generation equals to the charge carrier generation rate (i.e. $P(E) = 1$) [27, 36]. Effect of different values of $P(E)$ on *J-V* characteristics has been discussed later. The result of numerical simulation (red dotted marker) confirms the accuracy of our analytical expressions (solid blue line). This implies that reflection and interference effects in the multilayer stack have been incorporated accurately in Eq. (2.22), i.e. we have successfully developed a unified expression for *J-V* characteristics by merging optical phenomena (using transfer matrix method) directly into the electrical transport equations. Presence of optical parameters in Eqs. (2.12)-(2.17) indicate the generalized aspect of the developed model unlike the previous one [31] (where average value of the carrier generation rate was used). Any modification in the optical and/or electrical parameter values and the corresponding impact on the *J-V* characteristics can be described by the model directly.

Now, we investigate the validity of average generation rate approximation. Using the same parameters of Table 3.1, a study of the analytical model of Altazin *et al.* [31] is also shown in Figs. 3.1(a) and 3.1(b) (green dashed line) where the average carrier generation rate G_{avg} (Eq. (2.8)) is used. $P(E) = 1$ has been used for this case also. All the other optical and electrical parameter values have been kept same for precise comparison between the results of average and position dependent generation rate. However, these curves show considerable amount of deviations from the numerical simulation which is a consequence of ignoring the position dependency of generation rate. In other words, the previous model [31] cannot predict the photocurrent accurately due to the constant generation rate approximation. Since dark current plays notable role at the open circuit voltage (V_{oc}) region, the *J-V* curve becomes less dependent on carrier generation rate around V_{oc}. Therefore the *J-V* curves obtained from average carrier generation rate approximation [31] depict minor deviations from

numerical simulation as well as from our analytical model around the V_{oc} region (Figs. 3.1(a) and 3.1(b)). Our model and numerical simulation show V_{oc} = 0.59 V and J_{sc} = 96.46 A/m^2 for 100 nm case, while previous model shows V_{oc} = 0.59 V and J_{sc} = 93.36 A/m^2. On the other hand, for 120 nm case, our model and numerical simulation show V_{oc} = 0.6 V and J_{sc} = 89.23 A/m^2, while previous model shows V_{oc} = 0.6 V and J_{sc} = 85.47 A/m^2.

Table 3.1. Parameters used for calculating the organic solar cell characteristics shown in Figs. 3.1 to 3.10.

Parameter	Value
Dielectric constant (ε)	3×10^{-11} F/m
Effective bandgap (E_g)	1.0 eV
Effective density of states (N_c, N_v)	1×10^{26} m^{-3}
Electron mobility (μ_n)	3×10^{-7} m^2/V s
Hole mobility (μ_p)	2×10^{-8} m^2/V s
Temperature (T)	300 K

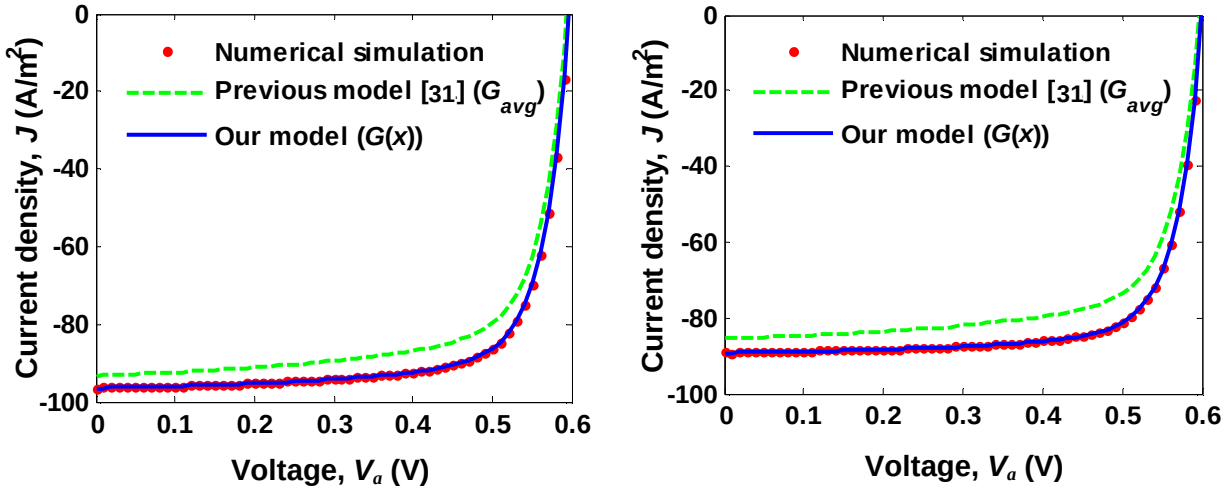

Fig. 3.1. *J-V* characteristics of the OSC for two active layer thicknesses: (a) d = 100 nm, (b) d = 120 nm. Our analytical model (solid blue line) considering position dependent carrier generation rate $G(x)$ is presented along with the numerical simulation (red dotted markers) and the previous model [31] considering average generation rate G_{avg} (dashed green line).

In addition, we have calculated the device efficiency[3] (for 100 nm and 120 nm thick active layers) using both the proposed model and the previous model [31]. The results from average carrier generation rate model have been compared with our model. A detail comparison is given in Table 3.2. The previous analytical model shows 7.764% (for 100 nm case) and 9.736% (for 120 nm case) deviation in efficiency from the proposed model (which considers spatial distribution of carrier generation rate). The maximum deviations in current density (in photovoltaic operating mode) for 100 nm and 120 nm thicknesses are 7.36 A/m^2 and 8.97 A/m^2, respectively. These results imply the importance of taking position dependent carrier generation in account for predicting accurate device performance.

Table 3.2. Percentage error[4] in predicting device efficiency using average generation rate model [31] from proposed model for 100 nm and 120 nm active layer thicknesses.

Thickness	Our model	Previous model [31]	
	Efficiency, η (%)	Efficiency, η (%)	Error (%)
100 nm	4.314	3.982	7.764
120 nm	4.062	3.667	9.736

3.1.2 Current-Voltage Characteristics from the Derived Model for Photovoltaic and Photo-Detector Modes

Another important aspect of our proposed model is wavelength dependent *J*-*V* characteristics (Eq. (2.22)). As a result, our model is also useful to study the device characteristics for a particular wavelength (λ) or wavelength band ($\Delta\lambda$). For example, we can use this model to study other photosensitive devices (e.g. light sensors based on organic photodiodes) as well. If we consider an

[3] To calculate the device efficiency, at first, we determine the power available from the device for different terminal voltages V_a. Next, we find the maximum power available from the device and divide it by the input sunlight power to obtain the device efficiency.

[4] Percentage error = $[(\eta_{\text{our model}} - \eta_{\text{previous model}})/\eta_{\text{our model}}]\times 100$ %

arbitrary monochromatic (λ = 400 nm) incident light beam of 100 Wm^{-2} intensity on our device structure (Fig. 2.1(a)), the consequent *J-V* characteristic obtained using our model is shown in Fig. 3.2 (solid blue line). The figure illustrates the *J-V* characteristic for both photovoltaic (solar cell) and photodiode (photo-detector) operating modes. Using average carrier generation rate, G_{avg} (Eq. (2.8)) into the previous analytical model [31] we obtain a *J-V* characteristic which is also shown in Fig. 3.2 (dashed green line). This curve shows major deviations from the solid blue line which again justifies the importance of considering position dependent generation rate similar to the earlier cases illustrated in Fig. 3.1. In this study, during the solar cell efficiency calculation, the model using average carrier generation rate approximation (dashed green line) shows 9.85% deviation from the case where spatial distribution of carrier generation rate has been considered (solid blue line).

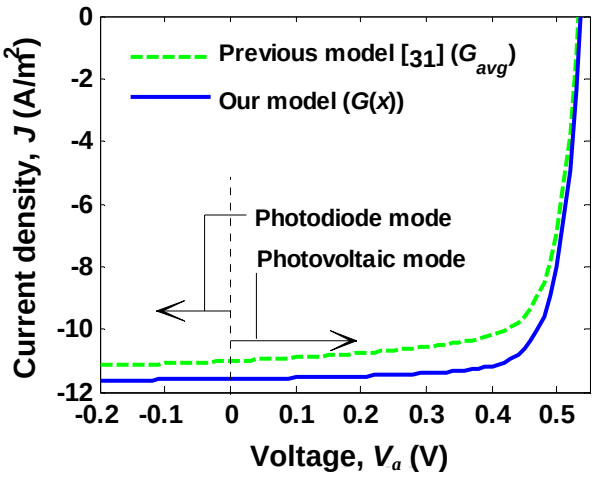

Fig. 3.2. *J-V* characteristics of the device for λ = 400 nm. Our analytical model (solid blue line) considering position dependent carrier generation rate $G(x)$ along with the previous model [31] considering average generation rate G_{avg} (dashed green line) for active layer thickness d = 100 nm.

3.1.3 Short Circuit Current Density (J_{sc}) for Different Active Layer Thicknesses (d)

To further validate and investigate the capability of our model, we have studied the short circuit current density (J_{sc}) for different active layer thicknesses which is shown in Fig. 3.3 along with the experimental data. Since the free charge carrier recombination terms have not been included in the

model, we cannot expect to describe the experimental data where free carrier recombination loss has been found significantly. However, due to the presence of various fitting parameters, it is possible to fit an experimental data without considering a particular physical phenomenon in a device model, although the phenomenon might have occurred in practical device operation. This issue will be discussed at the end of this section. We have taken the experimental data from Ref. [27] where authors find that the recombination phenomena is negligible for their P3HT:PCBM based device and ignore the recombination terms in their computation. They consider that e-h pair generation rate is equal to the charge carrier generation rate (i.e. $P(E) = 1$). Here, we investigate whether our derived expression can explain the experimental data without considering the free charge carrier recombination term either assuming $P(E) = 1$ as well . The device dimensions as well as the mobility parameter values have also been taken from Ref. [27]. Optical parameter values have been extracted from the work of Li *et al.* [23] since sufficient data are not given in Ref. [27]. The oscillation features in the experimental data [27] arise from the reflection and interference effects within the device structure [23]. It can be seen that our analytical model (solid blue line) follows the experimental data (red rectangles) with considerable accuracy. This implies that incorporating the position dependent generation rate in our optoelectronic model also accounts for the reflection and interference effects in different layers of the multilayer stack as it is expected from optical transfer matrix method. As the blend thickness is altered, light intensity within the device is redistributed due to the reflection and interference effects depending on different layers of the multilayer stack, which is modeled by the transfer matrix formalism. Redistribution of intensity can lead to increased or decreased photon absorption in the active layer [54]. Therefore, J_{sc} is changed at different blend thicknesses. Since transfer matrix formalism has been used directly to develop the expression of *J-V* characteristics (Eq. (2.22)), it is able to explain the enhanced J_{sc} at certain thicknesses. Each time the active layer thickness is changed, our derived expression directly shows the effect on *J-V* curve (Fig. 3.1), hence at the J_{sc} as well (Fig. 3.3). Assuming exponential decay of light intensity [34] (Beer-Lambert law), it is not possible to explain the oscillating nature of carrier generation rate and the similar trend of J_{sc}

for different thicknesses [23, 32]. Using Beer-Lambert law, instead of oscillation, Li *et al.* [23] observed exponential nature in the photon absorption vs different active layer thicknesses plot. Therefore, it is more appropriate to use optical transfer matrix method when the device layer thicknesses become less than the wavelength of incident light [32].

A simulation work (dashed green line) from Monestier *et al.* [27] is also given in Fig. 3.3. Our model shows good matching with the experimental data from 70 nm to 160 nm of active layer thickness whereas the previous simulation work shows notable deviations. However, we observe small deviations between the results of our model and the experimental data for active layer thicknesses above 200 nm. The deviation at higher thicknesses maybe due to the thickness dependence of optical constants (*n*,*k*) [27]. To investigate the exact cause of this deviation complementary study of optical constants on larger active layer thicknesses is required which is beyond the scope of this work [27].

It is noteworthy that theoretical study of short circuit current versus the active layer thickness has been done by several research groups [27, 28, 31] for this type of OSC and they have also found it difficult to bring the theoretical and experimental curves in closer agreement for different thicknesses. Sievers *et al.* [28] mentioned that a more rigorous fitting of the parameters and more accurate optical data might be helpful to lessen these deviations. However, typical active layer thicknesses generally used for P3HT:PCBM based BHJ OSC study in literature are approximately within the range of 70 nm to 160 nm for optimized performance [25, 26, 55-57] and our model shows acceptable results in this range. For considerable thicker layers, device efficiency decreases due to the substantial electrical losses in spite of improved light absorption. As a result, thick layers are not of practical interest [25, 31, 54]. On the contrary, excessive thin layers show high carrier collection efficiency at the cost of low light absorption. Therefore, researchers have been using optimum active layer thickness for increased photon absorption and reduced electrical losses [54, 58].

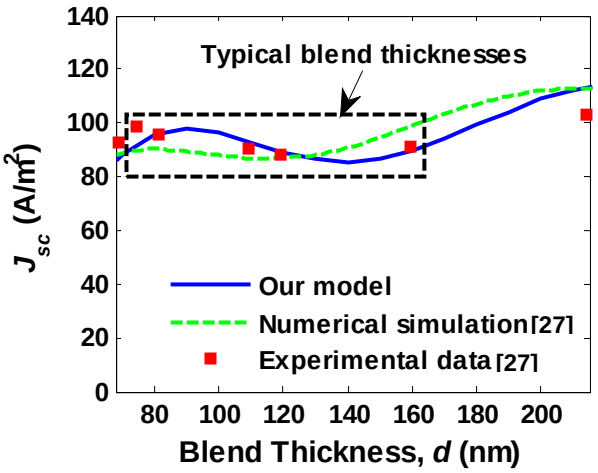

Fig. 3.3. Short circuit current density (J_{sc}) versus active layer thicknesses. Results obtained from our analytical model (solid blue line) and the numerical simulation done by Monestier *et al.* [27] (dashed green line). Red rectangles represent the experimental data [27].

3.1.4 Effect of e-h Pair Dissociation Probability *P*(*E*) on the *J*-*V* Characteristics

Figure 3.4(a) shows the effect of different values of e-h pair dissociation probability $P(E)$ on the *J*-*V* characteristics of BHJ solar cell. We have included this effect in our model using Eqs. (2.23)-(2.29). *J*-*V* curve for $P(E) = 1$ (Fig. 3.4(a) circular marker) refers to our earlier study in Fig. 3.1(a), i.e. the rate of exciton generation equals to the charge carrier generation rate [27, 36]. For the *J*-*V* curves represented by rectangular and triangular markers in Fig. 3.4(a), e-h pair separation distance has been assumed to be not constant in the active layer due to the disordered characteristics of BHJ structure (as mentioned earlier). For these cases, the term $p(a, E)$ [Eq. 2.26] has been integrated over a distribution of separation distances as expressed in Eq. (2.25). We can vary the value of e-h pair dissociation probability $P(E)$ using different values of fitting parameter k_f in Eq. (2.26) which represents the decay rate of the bound e-h pair to the ground state [26]. Other research groups [26, 28, 31] have also used k_f as a fitting parameter in their studies. If we increase the value of k_f, probability $P(E)$ decreases (Fig. 3.4(b) rectangular marker and triangular marker) as it is expected according to Eq. (2.26). Moreover, for a particular value of k_f, probability $P(E)$ decreases with the increase of terminal voltage V_a (Fig. 3.4(b)). In other words, $P(E)$ decreases with the decrease of electric field E.

Dependency of $P(E)$ on electric field is a consequence of field dependent dissociation rate $k_{diss}(a, E)$ in Eq. (2.26) [26]. For $k_f = 1.5\times10^6$ s^{-1} [26], $P(E)$ becomes 0.51 at the open circuit voltage region and 0.62 at the short circuit condition (Fig. 3.4(b) triangular marker). $P(E)$ values of similar range were also observed in the work of Koster *et al*. [26] for $k_f = 1.5\times10^6$ s^{-1}. In Eq. (2.27), $a_0 = 1.3$ nm [25, 26, 28] has been used for the study.

It can be noted that Refs. 26 and 28 have used distribution of e-h pair separation distances [Eq. (2.27)], i.e., they have assumed that e-h pair separation distance is not constant in the active layer. This procedure has been used for rectangular and triangular markers in Fig. 3.4. Recently, Trukhanov *et al*. [45] has also used this approach for their BHJ OSC studies. However, Refs. 25 and 31 have used constant e-h pair distance in their calculations. Since both approaches are available in literature, we present them in this work and compare the results. Now, we study the *J-V* characteristics of the device considering constant e-h pair distance ($a = a_0 = 1.3$ nm) [Fig. 3.4(a) dashed line, only shown for $k_f = 1.5\times10^6$ s^{-1} for clarity], i.e., we avoid the integration over a distribution of separation distances in Eq. (2.25). In other words, rather than assuming different separation distances, a constant value of e-h pair distance ($a = a_0$) has been used for the dashed line in Fig. 3.4(a) by following the procedure mentioned in the theory section. This *J-V* curve (Fig. 3.4(a) dashed line) shows significant deviation from the previous case (triangular marker) where e-h pair separation distance was considered as a non-constant quantity due to the disordered characteristics of the active layer blend [26, 28, 45]. We observe 17.5% deviation at the short circuit current. Corresponding dissociation probability is shown in Fig. 3.4(b) (dashed line). Thus, different results can be obtained depending on the consideration of e-h pair distance as a constant or non-constant term (by using a distribution of separation distances). Therefore, care should be taken about this issue while calculating or optimizing the device performance.

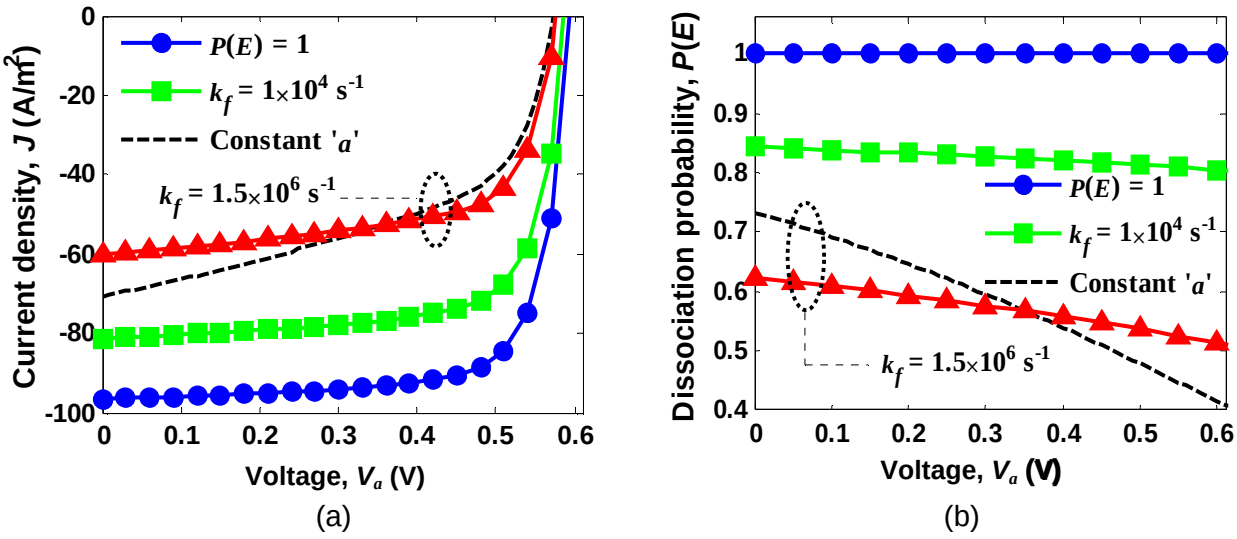

Fig. 3.4. (a) *J-V* characteristics of the OSC for $P(E)$=1 (circular marker) and for different values of k_f (rectangular marker, triangular marker and dashed line assuming constant e-h pair separation distance '$a = a_0$ = 1.3 nm' [only shown for $k_f = 1.5\times10^6$ s^{-1} for clarity]), (b) Dissociation probability for different voltages. $P(E)$=1 (circular marker), a constant value, similar to previous studies [27, 36] and the effect of k_f on $P(E)$ for different voltages (rectangular marker, triangular marker and dashed line assuming constant '$a = a_0$ = 1.3 nm' [only shown for $k_f = 1.5\times10^6$ s^{-1} for clarity]).

In total, $P(E)$ decreases with the increment of decay rate k_f, and eventually, the performance of the device degrades severely due to the low dissociation of e-h pair as shown in Fig. 3.4(a). Since the effect of $P(E)$ is only on the photo-generated carriers (Eqs. (2.23) and (2.24)), the *J-V* curve remains almost same at the V_{oc} as dark current plays dominating role at this region. This study implies that a significant improvement in device performance can be made by facilitating the bound e-h pair dissociation (i.e. by increasing the probability $P(E)$).

3.1.5 Power Conversion Efficiency for Different Active Layer Thicknesses

Using the proposed optoelectronic model, we have further studied the power conversion efficiency of the device for typical active layer thicknesses (Fig. 3.5 solid blue line). This plot also shows

oscillating nature due to the reflection and interference effects similar to the J_{sc} vs thickness study. We have included the e-h pair dissociation probability $P(E)$ in our calculation ($k_f = 1.5\times10^6$ s^{-1} has been used). The cell shows comparatively higher efficiency (around 2.27% to 2.31%) at the range of 80-100 nm active layer thicknesses [23, 59]. In general, for thicker active layers, $P(E)$ decreases due to their lower electric field. Thereby, carrier loss is increased and eventually the device performance degrades considerably [25, 31]. However, device performance can be different depending on the material purity, preparation condition and film morphology. Variation in device efficiency has been reported, even for very similar device architecture and preparation procedure [33]. If we replace the active layer with poly(3-hexylthiophene):[6,6]-phenyl-C_{71}-butyric acid methyl ester (P3HT:PC_{71}BM) blend (1:0.7 by weight ratio), the device performance improves significantly (Fig. 3.5 dashed green line) due to its better photon absorption property [60]. We have observed an upward shift of about 1.4% efficiency for different blend thicknesses as shown in Fig. 3.5. For 90 nm thick active layer, efficiency has increased from 2.31% to 3.74%.

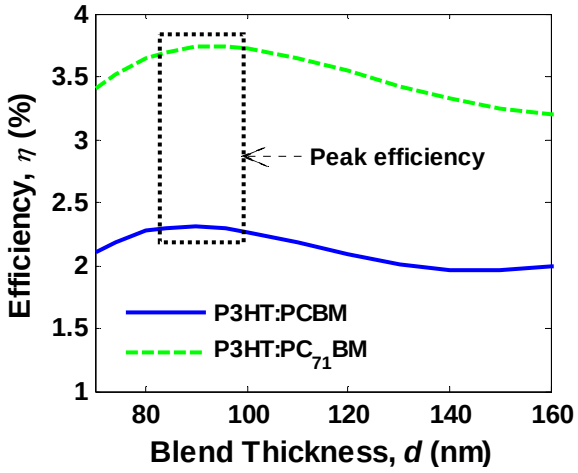

Fig. 3.5. Power conversion efficiency (η) versus active layer thicknesses for P3HT:PCBM (solid blue line) and P3HT:PC_{71}BM (dashed green line) based BHJ OSC.

Figure 3.6(a) shows the *J-V* characteristics of P3HT:PCBM and P3HT:PC_{71}BM blends for the active layer thickness of 90 nm (solid lines) and 120 nm (dashed lines). For P3HT:PCBM blend, when we

increase the thickness from 90 nm to 120 nm, J_{sc} is reduced from 62.37 A/m^2 to 53.92 A/m^2, while the fill factor and V_{oc} remain around 0.65 and 0.58 V, respectively. Thus, the change in conversion efficiency for different blend thicknesses majorly depends on the J_{sc}. Therefore, the device performance follows the oscillating trend of J_{sc} as we vary the active layer thickness (Fig. 3.5 solid blue line). Similar argument can be applied for the P3HT:PC_{71}BM blend also (Fig. 3.5 dashed green line). Figure 3.6(b) shows the improved photon absorption (ratio of absorbed photons to incident photons at different wavelengths) of P3HT:PC_{71}BM blend over P3HT:PCBM for 90 nm and 120 nm active layers, which increases the device efficiency significantly. As a result, the efficiency vs blend thickness curve shifts upward as shown in Fig. 3.5. For each of the blend type, as we go from 90 nm to 120 nm thick active layer, photon absorption is decreased (Fig. 3.6(b)) depending on the redistribution of light intensity as described earlier. This reduced absorption degrades the *J-V* characteristics (Fig. 3.6(a)) and eventually lowers the device performance (Fig. 3.5).

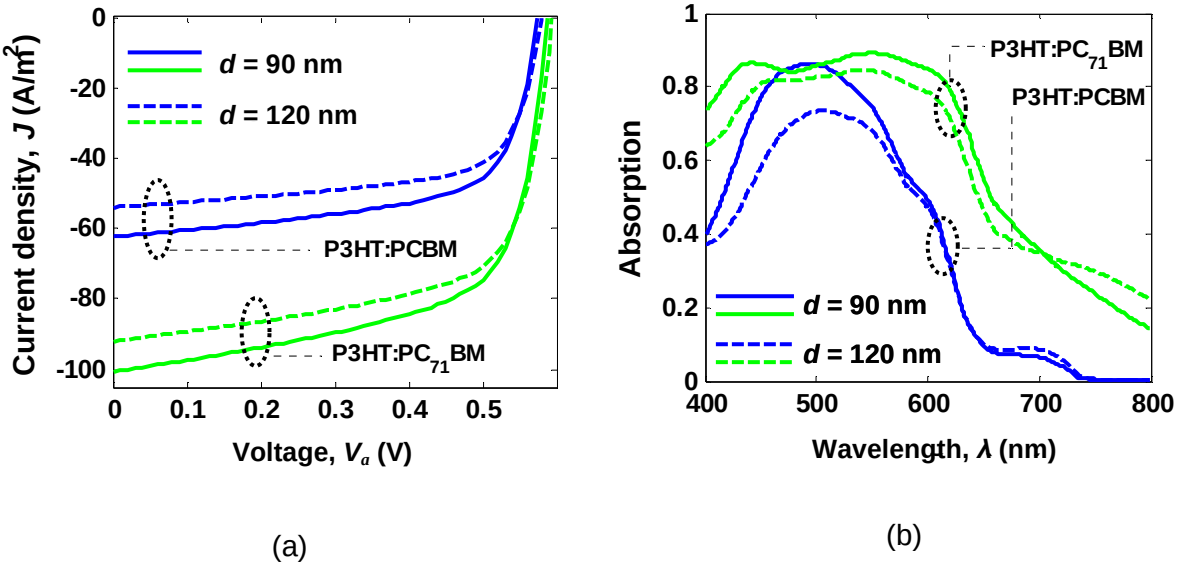

Fig. 3.6. (a) *J-V* characteristics of the OSC for P3HT:PCBM and P3HT:PC_{71}BM based blend. (b) Effect of P3HT:PCBM and P3HT:PC_{71}BM blend on photon absorption for 90 nm and 120 nm thick active layers.

3.1.6 Effect of Titanium Suboxide (TiO_x) Layer on Device Performance

To further demonstrate the capability of our model in device optimization, we have analyzed the modified device proposed recently by Roy *et al.* [54]. They have studied the effect of titanium suboxide (TiO_x) layer on their device performance (by including a 10 nm thick TiO_x layer as an optical spacer between the active layer and the metal contact Al). Here, in the same way, we introduce TiO_x layer (10 nm) in our device structure and investigate the effect of TiO_x on the efficiency using our developed model. Optical parameter values of TiO_x have been taken from Ref. [54]. The dashed line in Fig. 3.7(a) represents the device efficiency with 10 nm TiO_x layer. Inclusion of TiO_x layer changes the reflections and interferences within the device and eventually shifts the peak efficiency from the thick layer to the thinner layer. Similar shift in the photon absorption process was mentioned by Roy *et al.* [54]. Moreover, presence of TiO_x layer improves the device efficiency for active layer thicknesses less than 80 nm. In fact, device efficiency has been improved from 2.1% to 2.27% for 70 nm thick active layer due to the enhanced photon absorption (Fig. 3.7(b) dashed green line). The improvement in the device efficiency is majorly due to the increased J_{sc} (in this case, J_{sc} increases from 59 A/m^2 to 63 A/m^2, the fill factor and V_{oc} remain almost same around 0.63 and 0.57 V, respectively). In total, device performance can be improved considerably by using TiO_x layer without increasing the active layer thickness. This result will be particularly useful to the case (i.e. device sample) where thickness cannot be increased due to the detrimental effect of internal series resistance of the cell (which reduces the device efficiency) [54]. The efficiency starts to fall after 80 nm and decreases significantly at the 100-120 nm range (Fig. 3.7(a)) due to the diminishing effect of TiO_x layer on photon absorption (Fig. 3.7(b) dotted line) for these thicknesses. Similar results were observed by Roy *et al.* [54] for their device structure.

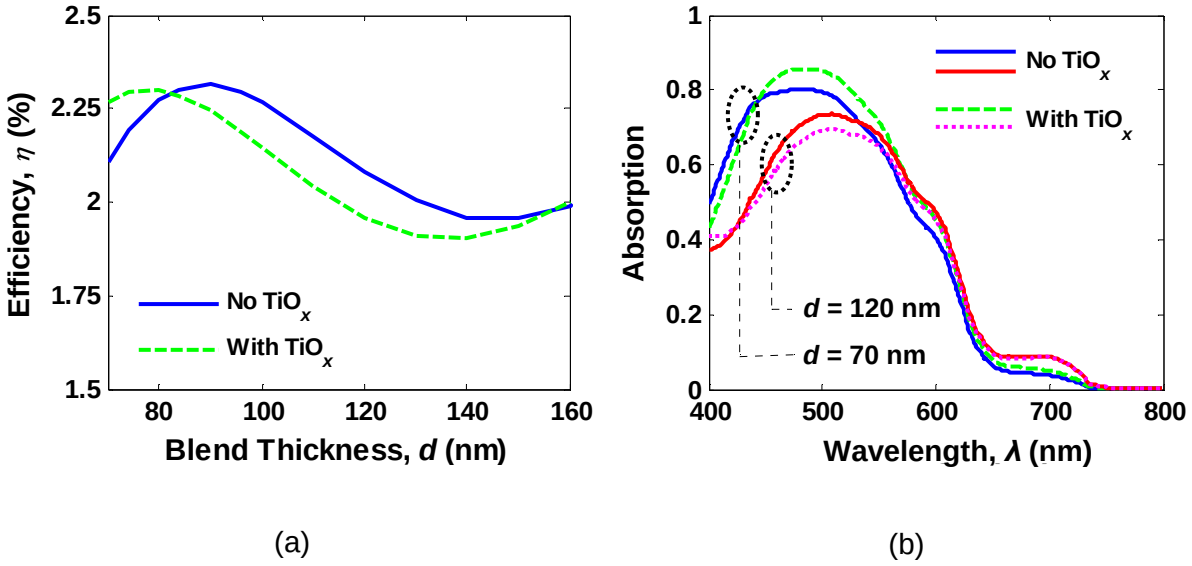

Fig. 3.7. (a) Power conversion efficiency (η) versus active layer thicknesses with and without TiO_x layer (dashed line and solid line, respectively). (b) Effect of TiO_x layer on photon absorption for 70 nm and 120 nm thick active layers.

3.1.7 Sensitivity of the Proposed Model

Next, we investigate the sensitivity of our proposed model to some input parameters. To do the sensitivity analysis, we alter different input parameter values and observe the variation at *J-V* curves. Four important input parameters - average e-h pair distance (a_0), e-h pair decay rate (k_f), electron mobility (μ_n) and hole mobility (μ_p) have been chosen to vary. All these parameters are directly related to the e-h pair dissociation probability [Eqs. (2.25)-(2.28)]. To conduct the analysis, a reference *J-V* curve was chosen. Then we change different parameter values and obtain new *J-V* curves. Afterwards, the reference curve is subtracted from the obtained *J-V* curves and eventually we find the sensitivity of current density for different voltages. Similar procedure was followed by Hausermann *et al.* [25] for the sensitivity analysis.

Firstly, we consider the *J-V* curve represented by dashed line in Fig. 3.4(a) as the reference curve, i.e., we have assumed a constant value for e-h pair distance ($a = a_0 = 1.3$ nm) rather than using the distribution given in Eq. (2.27). We have varied the a_0 parameter value by ±3%, and the μ_n and μ_p parameter values by ±10%. Wide range of k_f parameter values have been used in literature, even for same BHJ materials. For example, Hausermann *et al.* [25] has used $k_f = 1\times10^5$ s^{-1} for a P3HT:PCBM blend, while Trukhanov *et al.* [45] has used $k_f = 1\times10^4$ s^{-1} for their P3HT:PCBM based BHJ OSC. Therefore, we have varied the k_f parameter value by a larger quantity (by ±20%) than the other three parameters. Effects of these variations on the reference *J-V* curve have been shown in Fig. 3.8(a) by the means of sensitivity of current density vs voltage curve. The negative and positive sensitivity in the figure refers to the increase and decrease from the reference current density, respectively. The average e-h pair distance a_0 has the highest influence on the curve (about 5 A/m^2 variation) [Fig 3.8(a) solid and dashed blue lines], although we changed the parameter value by ±3% only. The e-h pair decay rate k_f has also significant influence on the curve (solid and dashed green lines). For ±20% variation of k_f parameter value, current density shows about 4 A/m^2 change from the reference. The effects of mobility parameter variations on the *J-V* curve are also shown in Fig. 3.8(a) [red lines (solid and dashed) and black lines (solid and dashed)]. It can be seen from the figure (dashed red line) that when we decrease the electron mobility value by 10%, current density is reduced till the V_{oc} region. However, at a certain point the sensitivity curve crosses the zero line and starts to indicate improved current density. It implies that the changed *J-V* characteristic (which shows reduced current density up to around 0.5 V) crosses the reference *J-V* curve at a particular point (before the reference V_{oc}), and subsequently starts to improve compared to the reference, i.e., the V_{oc} has been increased due to the lowering of mobility value, although the J_{sc} has been decreased. Similar phenomena have been reported by Shieh *et al.* [61]. Using analogous arguments, effects of other mobility parameters on the reference *J-V* curve can be explained. Although the variations of a_0 and k_f alter the magnitude of current density significantly [Fig. 3.8(a) blue lines (solid and dashed) and green lines (solid and dashed)], they do not influence J_{sc} and V_{oc} differently as the mobility parameter variations do (e.g. J_{sc}

decreases while V_{oc} increases when we lower the μ_n value by 10%). Therefore, the blue and green lines in Fig. 3.8(a) do not show any dramatic variation (i.e. transition from positive to negative or negative to positive) for different voltages as it has been observed for mobility variation cases [red lines (solid and dashed) and black lines (solid and dashed)]. However, for the model which takes free charge carrier recombination phenomena into account, the considered parameters may affect the *J-V* characteristics differently depending on the amount of recombination.

From Fig. 3.8(a), it can be seen that the slight change in different parameter values can alter the current density significantly, which gives wide options to fit a curve. For example, Ref. [31] has not considered recombination of free charge carriers in their model. They have included only e-h pair dissociation probability in the calculation. Using their derived model (and assuming a constant value for carrier generation rate), they have matched a published experimental data presented by Koster *et al.* [26]. However, Koster *et al.* [26] described their data by using considerable recombination (bimolecular recombination) of free carriers in the calculation. Hence, it is possible to fit an experimental *J-V* curve data points by considering both e-h pair dissociation probability and free charge carrier recombination phenomena [26], while the same data points can be fitted by varying different parameter values slightly and taking the e-h pair dissociation probability in calculation only (without considering free charge carrier recombination) [31]. Therefore, ability to fit an experimental *J-V* curve by ignoring free charge carrier recombination phenomena in a model does not necessarily imply that the recombination among the free carriers was absent or negligible in the device operation.

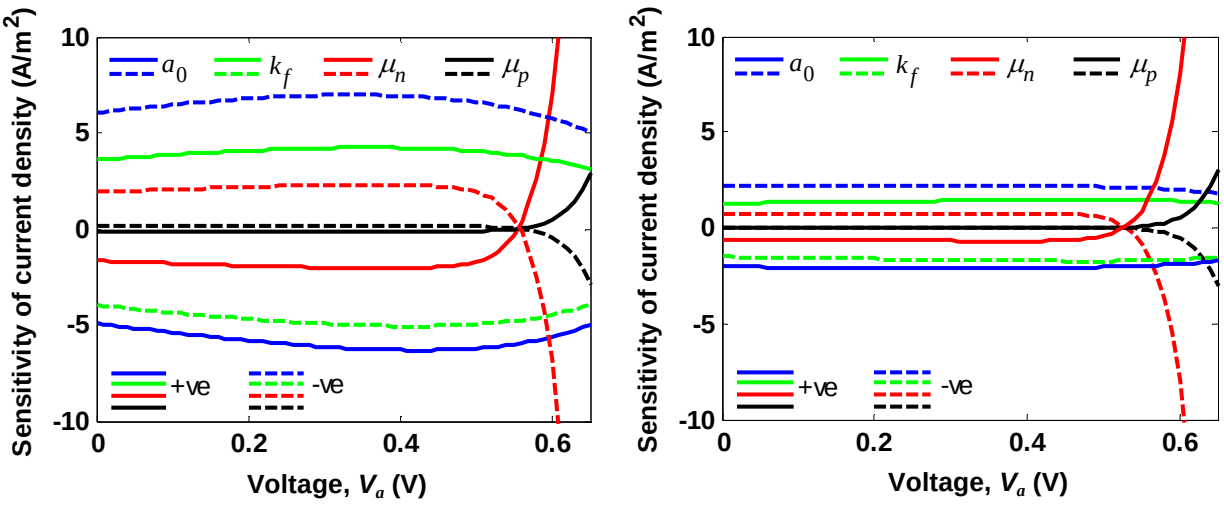

Fig. 3.8. Sensitivity of the current density in a *J-V* curve (a) for constant '*a*' (b) for non-constant '*a*'. a_0, k_f, μ_n and μ_p parameter values have been varied by ±3% (blue lines), ±20% (green lines), ±10% (red lines) and ±10% (black lines), respectively. Solid lines represent the positive variations (+ve) of the parameter values while the dashed lines represent the negative variations (-ve).

Next, we considered the *J-V* curve represented by triangle marker in Fig. 3.4(a) as the reference curve, i.e., using the distribution given by Eq. (2.27) rather than assuming a constant value for e-h pair distance. For this case also, we have varied the same parameter (a_0, k_f, μ_n and μ_p) values in a similar manner. Figure 3.8(b) shows the obtained results. It is apparent that the model shows less sensitivity (almost half compared to the previous case) to the variation of considered parameters when we use the distribution function [Eq. (2.27)] in our model. Since the parameters are related to each other through the Eqs. (2.25)-(2.28), all of them are responding to the inclusion of distribution function [Eq. (2.27)] and eventually influencing the *J-V* curve to a lesser extent [Fig. 3.8(b)]. Therefore, the model could show different sensitivity depending on whether we consider the e-h pair distance as a constant quantity or not in the active layer.

3.2 Results Obtained from the Empirical $G(x)$ Based OSC Model

3.2.1 Proposed Empirical Expression of Carrier Generation Rate Describing Published Data

Here, we investigate whether our proposed empirical expression is capable to describe the carrier generation rate profile extracted from a published work [27], where the authors have used complicated numerical simulations to calculate the electromagnetic field and the carrier generation within the OSC. Spatial distributions of carrier generation rate for different blend thicknesses (60, 100, 140 and 200 nm) are shown in Fig. 3.9 (red rectangles). Due to the consideration of interference effects, the profiles show oscillating behavior unlike the conventional solar cells where Beer-Lambert law is often used to describe the exponential decay of light intensity in bulk materials [23]. Since the thickness of different layers in OSC is generally less than the wavelength of incident light, the optical effects such as reflections and interference become important to take into consideration for predicting the device performance more accurately [23,27].

Figure 3.9 shows that our empirical expression [Eq. (2.31)] (solid blue line) successfully follows the profiles given by Monestier *et al*. [27] (red rectangular marker) for different thicknesses. The fitting parameters a_m, b_m and c_m are given in Appendix A (Table A.1). Since the active layer thickness is in nanometer range (typically < 200 nm), the magnitude of carrier generation rate profile does not change by large factors with respect to position (Fig. 3.9). This particular result allows us to fit the generation rate profiles using the sum of few sine functions[5] as stated in Eq. (2.31). Otherwise, if the active layer thickness were in μm range, the generation rate profile would decay exponentially with respect to position [23]. For this case, the expression given by Furlan and Amon [13] in Eq. (2.30) would be more appropriate. However, thick blend layers in BHJ OSC are not of practical interest [23], since electrical losses increase with the increment of blend thickness and eventually the device

[5] For the present case, sum of five sine functions are found to be enough for the fitting purpose as shown in Fig. 3.9.

efficiency is deteriorated significantly [23,26,31]. Therefore, the proposed expression [Eq. (2.31)] will be more appropriate for the thin film based structure of OSC. Oscillation feature of carrier generation profile is also found in bilayer organic solar cells as well as in other thin film based solar cells [23,32]. Our generalized empirical formula can be used to obtain the analytical model of these devices also.

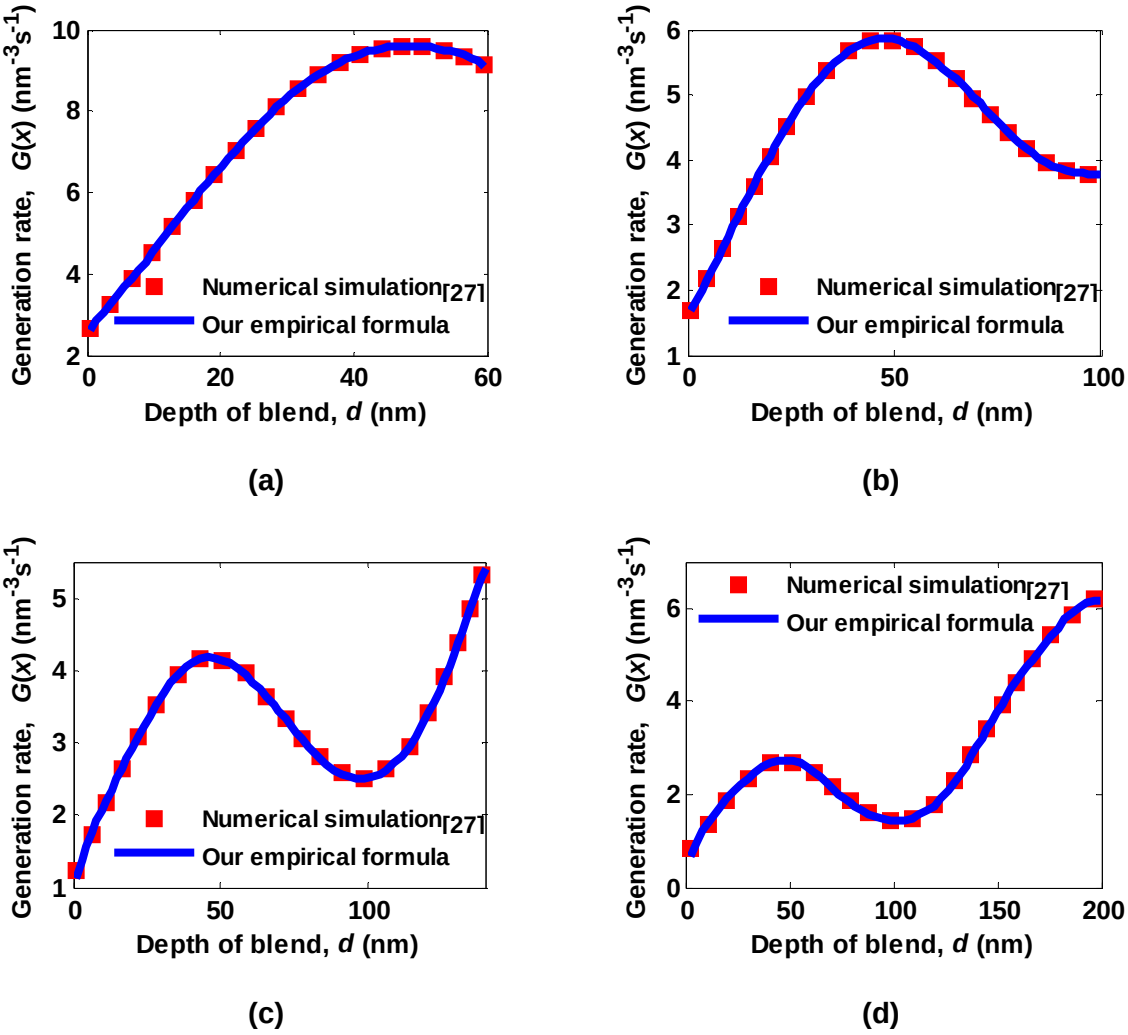

Fig. 3.9. Profiles of carrier generation rate for various active layer thicknesses (a) 60 nm, (b) 100 nm, (c) 140 nm and (d) 200 nm. Solid blue lines represent the results obtained from our proposed empirical expression [Eq. (2.31)] and red rectangular markers represent the result of the numerical simulations in Ref. [27].

3.1.2 Current-Voltage Characteristics from the Derived Model and Comparison with Numerical Simulations

Figure 3.10 shows *J-V* characteristics obtained from our analytical model (solid green line) [derived in section 2.2] along with the results of numerical study (rectangular marker) done in this work. Figures 3.10(a)-3.10(d) demonstrate the study for 60, 100, 140 and 200 nm thick active layers, respectively.

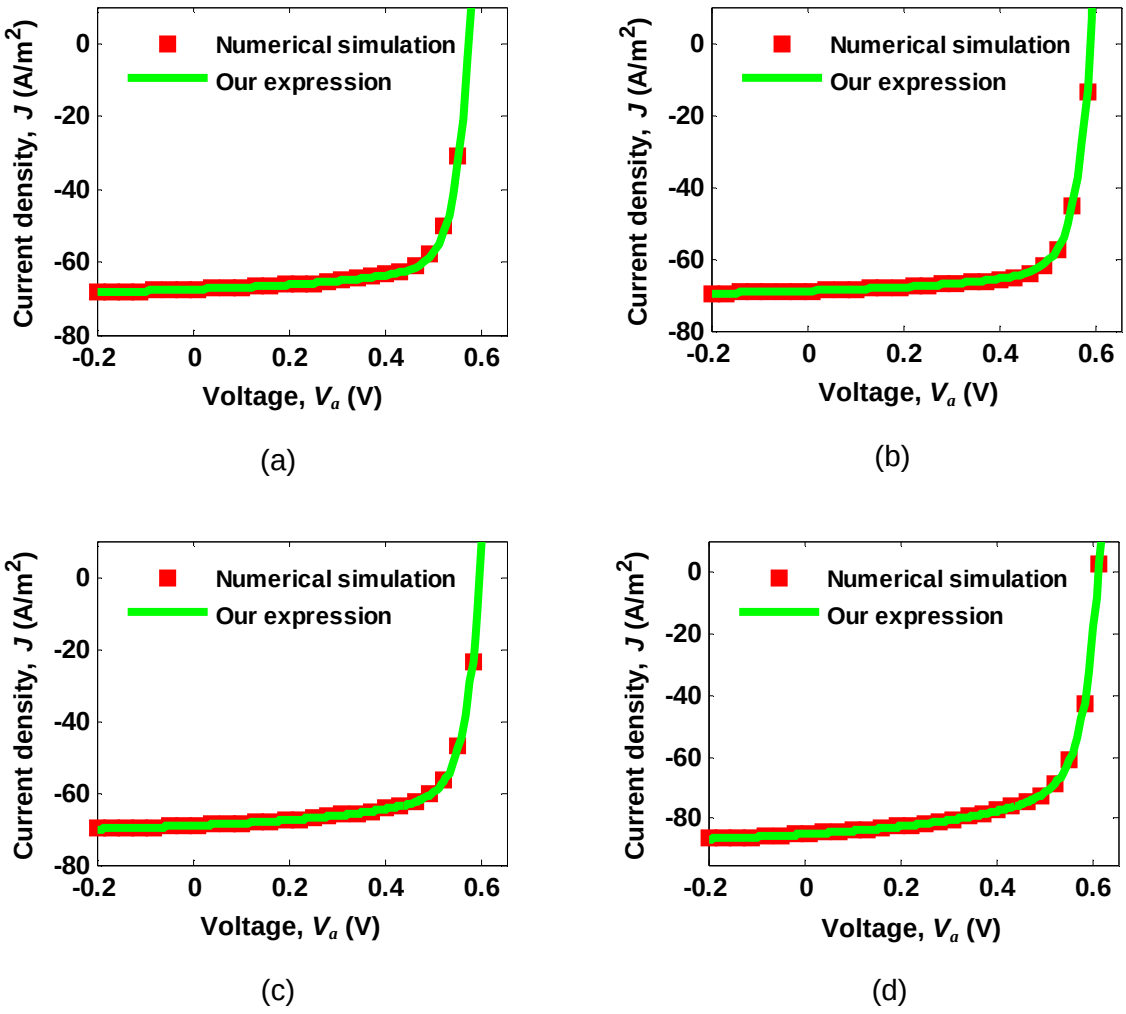

Fig. 3.10. *J-V* characteristics of the considered OSC for four different active layer thicknesses (a) 60 nm, (b) 100 nm, (c) 140 nm and (d) 200 nm. Solid green lines represent the results obtained from our derived analytical model in section 2.2 and red rectangular markers represent the result of the numerical simulations.

The parameters used in this study are given in Table 3.1. The fitting parameter values (a_m, b_m and c_m) of empirical expression [Eq. (2.31)] have been taken from Appendix A (Table A.1). For numerical simulation we have solved the Eqs. (2.32) and (2.33) using Finite Element Method [53] and used the generation rate data directly from the work of Monestier *et al.* [27]. The result of numerical simulation (rectangular marker) confirms the correctness of our analytical expressions (solid green lines). It also justifies the accuracy of our proposed empirical expression for the space dependent carrier generation rate profile.

3.2.3 Power Conversion Efficiency for Different Active Layer Thicknesses

Figure 3.11 shows device efficiencies for different blend thicknesses (60, 100, 140 and 200 nm). Our derived model (solid blue circles) shows good agreement with the numerical simulations (red rectangular marker), which justifies our proposed empirical expression for carrier generation rate profile as well as the OSC device model derived in section 2.2.

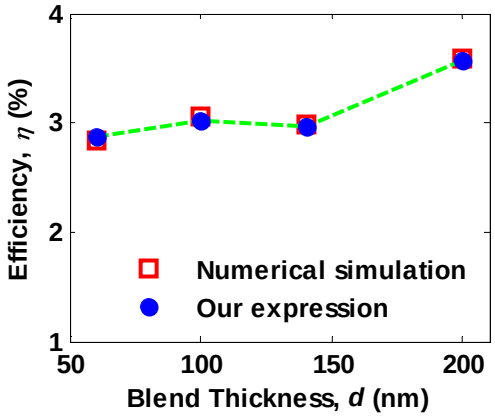

Fig. 3.11. Power conversion efficiency (η) for four different active layer thicknesses (60, 100, 140 and 200 nm). Solid blue circles represent our analytical model while red rectangular markers stand for the numerical simulations. The dashed green line shown represents a guide to the eye, rather than model results.

It can be seen that the device conversion efficiency vs blend thickness curve shows an oscillating pattern. Similar pattern was observed in Fig. 3.5 also (in section 3.1.5). The pattern can be explained by the same argument as it was mentioned in section 3.1.5, i.e., the change in conversion efficiency for different blend thicknesses majorly depends on the J_{sc}. Therefore, the device performance follows the oscillating trend of J_{sc} as we vary the active layer thickness.

Chapter 4

Conclusions & Future Works

4.1 Conclusions

We have merged the optical and electrical phenomena into a single unified expression of *J-V* characteristics of BHJ OSC. We have applied optical transfer matrix theory into the electrical transport equations to describe the *J-V* characteristics. Hence our model is capable of dealing with interference and reflection effects in different layers of the device structure. This analytical model accounts the position dependent carrier generation rate, which had been neglected in previous analytical models as well as in few numerical models. We have found that the position dependency of carrier generation rate has notable impact on the *J-V* characteristics. It is important to consider spatial distribution of carrier generation rate within the active layer to predict device performance more accurately. Furthermore, because of the wavelength dependent photocurrent expression, the model can be used to study the performance of the device at a particular wavelength or wavelength band. The model shows excellent agreement with the numerical results and published experimental data. Since optical transfer matrix method has been used to develop the model, it is capable to describe the enhanced short circuit current density for certain active layer thicknesses. In addition, e-h pair dissociation probability has been included in the model, and the effect of this probability on the device performance has been studied. Depending on whether we consider the e-h pair distance as a constant or non-constant term during the dissociation probability calculation, J_{sc} shows significant variation (17.5% for the considered case). Therefore, this issue also requires enough attention while calculating or optimizing the device performance. We have also described the effect of different layer thicknesses on the device power conversion efficiency. In short, our model would be instrumental in predicting the *J-V* characteristics of BHJ OSC and devices like photo-detectors more realistically than

the previous analytical models do without numerical computational complexities. Therefore, it would be effective in understanding and optimizing such devices.

In addition, we have found that a sum of sine functions can be used to approximate the spatial distribution of carrier generation rate in OSC. Interestingly, this single empirical formula is capable to follow the generation rate for different thicknesses. This approach is especially useful to the cases where carrier generation rate cannot be described by any physics-based closed form expression, and the only way to develop the OSC device model is by following an empirical expression which can model the spatial distribution of generation rate profile directly obtained from experimental data, complicated numerical simulations or any other published data. Previous empirical expression for traditional solar cells is unable to fit the carrier generation profile in thin film based OSC structures. We have incorporated the proposed empirical expression into the carrier transport equations to model the BHJ OSC *J-V* characteristic. This analytical model is capable of considering position dependency of carrier generation rate in a very simple and straightforward way. The obtained results confirm exact match with numerical simulations and published data. In total, the proposed empirical formula of carrier generation rate as well as the derived analytical model will be helpful to obtain physical insight into the device performance in a straightforward way by avoiding any complicated numerical calculations.

4.2 Suggestions for Future Works

An interesting contribution would be to incorporate carrier recombination phenomena properly in the developed models. Another obvious extension of this work would be to study the effect of different parameter values on the device performance and to compare the outcome with numerical simulations. A comparative study between the OSC models originated from Beer-Lambert law and transfer matrix formalism could also be done. Although, the models in this thesis have been developed for BHJ

organic solar cells, the insight gained from this work can be adopted to model other thin film based solar cells as well.

References

[1] Yu, G., Gao, J., Hummelen, J. C., Wudl, F., Heeger, A. J., "Enhanced efficiencies via a network of internal donor-acceptor heterojunctions", *Science-AAAS-Weekly Paper Edition*, vol. 270, pp. 1789-1790, 1995.

[2] Krebs, F.C., "Fabrication and processing of polymer solar cells: a review of printing and coating techniques", *Sol. Energy Mater. Sol. Cells*, vol. 93, pp. 394-412, 2009.

[3] Houghton, J. T., "Climate change 1995: The science of climate change: contribution of working group I to the second assessment report of the Intergovernmental Panel on Climate Change", Cambridge University Press, 1996.

[4] Watson, R. T., Zinyowera, M. C., and Moss, R. H., "The regional impacts of climate change: an assessment of vulnerability", Cambridge University Press, 1998.

[5] Flavin, C. and Dunn, S., "A new energy paradigm for the 21st century", *Journal of International Affairs*, vol. 53, pp. 167-190, 1999.

[6] Becquerel, A. E., "Mémoire sur les effets électriques produits sous l'influence des rayons solaires", *Comptes Rendus des Séances Hebdomadaires*, vol. 9, pp. 561-567, 1839.

[7] Chapin, D. M., Fuller, C. S., and Pearson, G. L., "A new silicon p-n junction photocell for converting solar radiation into electrical power", *J. Appl. Phys.*, vol. 25, pp. 676-677, 1954.

[8] Wind in Power: 2011 European Statistics, The European Wind Energy Association, see http://www.ewea.org/statistics/european/

[9] Krebs, F. C., Hösel, M., Corazza, M., Roth, B., Madsen, M. V., Gevorgyan, S. A., Søndergaard, R. R., Karg, D. and Jørgensen, M., "Freely available OPV—The fast way to progress", *Energy Technology*, vol. 1, pp. 378–381, 2013.

[10] Cummerow, R. L., "Photovoltaic Effect in p-n Junctions", *Phys. Rev.*, vol. 95, p. 16, 1954.

[11] Fonash, S., *Solar cell device physics*, second ed., Elsevier, 2012.

[12] PV EDUCATION.ORG, see http://www.pveducation.org/pvcdrom.

[13] Furlan, J. and Amon, S., “Approximation of the carrier generation rate in illuminated silicon”, *Solid-state electronics*, vol. 28, pp. 1241-1243, 1985.

[14] Krebs, F. C., “All solution roll-to-roll processed polymer solar cells free from indium-tin-oxide and vacuum coating steps”, *Organic Electronics*, vol. 10, pp. 761-768, 2009.

[15] Zimmermann, B., Glatthaar, M., Niggemann, M., Riede, M. K., Hinsch, A., and Gombert, A., “ITO-free wrap through organic solar cells - a module concept for cost-efficient reel-to-reel production”, *Sol. Energy Mater. Sol. Cells*, vol. 91, pp. 374-378, 2007.

[16] Zimmermann, B., Würfel, U., and Niggemann, M., “Longterm stability of efficient inverted P3HT: PCBM solar cells”, *Sol. Energy Mater. Sol. Cells*, vol. 93, pp. 491-496, 2009.

[17] Manceau, M., Angmo, D., Jørgensen, M., and Krebs, F. C., “ITO-free flexible polymer solar cells: from small model devices to roll-to-roll processed large modules”, *Organic Electronics*, vol. 12, pp. 566-574, 2011.

[18] Brabec, C.J., Gowrisanker, S., Halls, J.J.M., Laird, D., Jia, S., and Williams, S.P., “Polymer–fullerene bulk-heterojunction solar cells”, *Advanced Materials*, vol. 22, pp. 3839-3856, 2010.

[19] Ameri, T., Dennler, G., Lungenschmied, C., and Brabec, C.J., “Organic tandem solar cells: a review”, *Energy & Environmental Science*, vol. 2, pp. 347-363, 2009.

[20] Pivrikas, A., Sariciftci, N. S., Juška, G., and Österbacka, R., “A review of charge transport and recombination in polymer/fullerene organic solar cells”, *Progress in Photovoltaics: Research and Applications*, vol. 15, pp. 677-696, 2007.

[21] Krebs, F.C., “Fabrication and processing of polymer solar cells: a review of printing and coating techniques”, *Sol. Energy Mater. Sol. Cells*, vol. 93, pp. 394-412, 2009.

[22] Kippelen, B., and Brédas, J.-L., “Organic photovoltaics”, *Energy Environ. Sci.*, vol. 2, pp. 251-261, 2009.

[23] Li, G., Liu, L., Wei, F., Xia, S., and Qian, X, “Recent progress in modeling, simulation, and optimization of polymer solar cells”, *IEEE J. Photovolt.*, vol. 2, pp. 320-340, 2012.

[24] Park, S.H., Roy, A., Beaupré, S., Cho, S., Coates, N., Moon, J.S., Moses, D., Leclerc, M., Lee, K., and Heeger, A.J., "Bulk heterojunction solar cells with internal quantum efficiency approaching 100%", *Nat. Photon.*, vol. 3, pp. 297-302, 2009.

[25] Hausermann, R., Knapp, E., Moos, M., Reinke, N.A., Flatz, T., and Ruhstaller, B., "Coupled optoelectronic simulation of organic bulk-heterojunction solar cells: Parameter extraction and sensitivity analysis", *J. Appl. Phys.*, vol. 106, pp. 104507-1-104507-9, 2009.

[26] Koster, L.J.A., Smits, E.C.P., Mihailetchi, V.D., and Blom, P.W.M., "Device model for the operation of polymer/fullerene bulk heterojunction solar cells", *Phys. Rev. B*, vol. 72, pp. 085205-1-085205-9, 2005.

[27] Monestier, F., Simon, J.-J., Torchio, P., Escoubas, L., Flory, F., Bailly, S., de Bettignies, R., Guillerez, S., and Defranoux, C., "Modeling the short-circuit current density of polymer solar cells based on P3HT: PCBM blend", *Sol. Energy Mater. Sol. Cells*, vol. 91, pp. 405-410, 2007.

[28] Sievers, D.W., Shrotriya, V., and Yang, Y., "Modeling optical effects and thickness dependent current in polymer bulk-heterojunction solar cells", *J. Appl. Phys.*, vol. 100, pp. 114509-1-114509-7, 2006.

[29] Marsh, R.A., McNeill, C.R., Abrusci, A., Campbell, A.R., and Friend, R.H., "A unified description of current–voltage characteristics in organic and hybrid photovoltaics under low light intensity", *Nano Lett.*, vol. 8, pp. 1393-1398, 2008.

[30] Kumar, P., Jain, S.C., Kumar, V., Chand, S., and Tandon, R.P., "A model for the *J-V* characteristics of P3HT: PCBM solar cells", *J. Appl. Phys.*, vol. 105, pp. 104507-1-104507-6, 2009.

[31] Altazin, S., Clerc, R., Gwoziecki, R., Pananakakis, G., Ghibaudo, G., and Serbutoviez, C., "Analytical modeling of organic solar cells and photodiodes", *Appl. Phys. Lett.*, vol. 99, pp. 143301-1-143301-3, 2011.

[32] Pettersson, L.A.A., Roman, L.S., and Inganas, O., "Modeling photocurrent action spectra of photovoltaic devices based on organic thin films", *J. Appl. Phys.*, vol. 86, pp. 487-496, 1999.

[33] Ng, A., Liu, X., Jim, W.Y., Djurišić, A.B., Lo, K.C., Li, S.Y., and Chan, W.K., "P3HT: PCBM solar cells—The choice of source material", *J. Appl. Polym. Sci.*, vol. 131, pp. 39776, 2014.

[34] Arnab, S.M., and Kabir, M.Z., "An analytical model for analyzing the current-voltage characteristics of bulk heterojunction organic solar cells", *J. Appl. Phys.*, vol. 115, pp. 034504-1-034504-7, 2014.

[35] Chowdhury, M.M., and Alam, M.K., "A physics-based analytical model for bulk heterojunction organic solar cells incorporating monomolecular recombination mechanism", *Curr. Appl. Phys.*, vol. 14, pp. 340-344, 2014.

[36] Liu, L., and Li, G., "Investigation of recombination loss in organic solar cells by simulating intensity-dependent current–voltage measurements", *Sol. Energy Mater. Sol. Cells*, vol. 95, pp. 2557-2563, 2011.

[37] Li, G., and Liu, L., "Carbon nanotubes for organic solar cells", *IEEE Nanotechnol. Mag.*, vol. 5, pp. 18-24, 2011.

[38] Brown, T.M., Kim, J.S., Friend, R.H., Cacialli, F., Daik, R., and Feast, W.J., "Built-in field electroabsorption spectroscopy of polymer light-emitting diodes incorporating a doped poly (3, 4-ethylene dioxythiophene) hole injection layer", *Appl. Phys. Lett.*, vol. 75, pp. 1679-1681, 1999.

[39] Sze, S.M., *Physics of semiconductor devices*, second ed., John Wiley & Sons, New York, 1981.

[40] Pulfrey, D.L., *Understanding modern transistors and diodes*, Cambridge University Press, New York, 2010.

[41] Street, R.A., Song, K.W., Northrup, J.E., and Cowan, S., "Photoconductivity measurements of the electronic structure of organic solar cells", *Phys. Rev. B*, vol. 83, pp. 165207-1-165207-13, 2011.

[42] Blakesley, J.C., and Neher, D., "Relationship between energetic disorder and open-circuit voltage in bulk heterojunction organic solar cells", *Phys. Rev. B*, vol. 84, pp. 075210-1-075210-12, 2011.

[43] Shuttle, C.G., Hamilton, R., Nelson, J., O'Regan, B.C., and Durrant, J.R., "Measurement of charge-density dependence of carrier mobility in an organic semiconductor blend", *Adv. Funct. Mater.*, vol. 20, pp. 698-702, 2010.

[44] Ballantyne, A.M., Chen, L., Dane, J., Hammant, T., Braun, F.M., Heeney, M., Duffy, W., McCulloch, I., Bradley, D.D.C., and Nelson, J., "The effect of poly(3-hexylthiophene) molecular weight on charge transport and the performance of polymer:fullerene solar cells", *Adv. Funct. Mater.*, vol. 18, pp. 2373-2380, 2008.

[45] Trukhanov, V.A., Bruevich, V.V., and Paraschuk, D.Y., "Effect of doping on performance of organic solar cells", *Phys. Rev. B*, vol. 84, pp. 205318-1-205318-14, 2011.

[46] Nam, Y.M., Huh, J., and Jo, W.H., "Optimization of thickness and morphology of active layer for high performance of bulk-heterojunction organic solar cells", *Sol. Energy Mater. Sol. Cells*, vol. 94, pp. 1118-1124, 2010.

[47] Cowan, S.R., Roy, A., and Heeger, A.J., "Recombination in polymer-fullerene bulk heterojunction solar cells", *Phys. Rev. B*, vol. 82, pp. 245207-1-245207-10, 2010.

[48] Fonash, S., Solar cell device physics, second ed., Elsevier, 2012.

[49] Mihailetchi, V.D., Wildeman, J., and Blom, P.W.M., "Space-charge limited photocurrent", *Phys. Rev. Lett.*, vol. 94, pp. 126602-1-126602-4, 2005.

[50] Kotlarski, J.D., and Blom, P.W.M., "Impact of unbalanced charge transport on the efficiency of normal and inverted solar cells", *Appl. Phys. Lett.*, vol. 100, pp. 013306-1-013306-3, 2012.

[51] Onsager, L., "Initial recombination of ions", *Phys. Rev.*, vol. 54, pp. 554-557, 1938.

[52] Braun, C.L., "Electric field assisted dissociation of charge transfer states as a mechanism of photocarrier production", *J. Chem. Phys.*, vol. 80, pp. 4157-4161, 1984.

[53] Comsol Inc., Comsol Multiphysics 3.5a, 2008, see http://www.comsol.com.

[54] Roy, A., Park, S. H., Cowan, S., Tong, M.H., Cho, S., Lee, K., and Heeger, A.J., "Titanium suboxide as an optical spacer in polymer solar cells", *Appl. Phys. Lett.*, vol. 95, pp. 013302-1-013302-3, 2009.

[55] Chou, C.H., Kwan, W.L., Hong, Z., Chen, L.M., and Yang, Y., “A metal-oxide interconnection layer for polymer tandem solar cells with an inverted architecture”, *Adv. Mater.*, vol. 23, pp. 1282-1286, 2011.

[56] Boix, P.P., Garcia-Belmonte, G., Muñecas, U., Neophytou, M., Waldauf, C., and Pacios, R., “Determination of gap defect states in organic bulk heterojunction solar cells from capacitance measurements”, *Appl. Phys. Lett.*, vol. 95, pp. 233302-1-233302-3, 2009.

[57] Liang, C.-W., Su, W.-F., and Wang, L., “Enhancing the photocurrent in poly (3-hexylthiophene)/[6, 6]-phenyl C_{61} butyric acid methyl ester bulk heterojunction solar cells by using poly (3-hexylthiophene) as a buffer layer”, *Appl. Phys. Lett.*, vol. 95, pp. 133303-1-133303-3, 2009.

[58] Shen, H., Bienstman, P., and Maes, B., “Plasmonic absorption enhancement in organic solar cells with thin active layers”, *J. Appl. Phys.*, vol. 106, pp. 073109-1-073109-5, 2009.

[59] Kim, K.-H., and Park, Q.H., “Maximal light-energy transfer through a dielectric/metal-layered electrode on a photoactive device”, *Opt. Express*, vol. 22, pp. 1963-1970, 2014.

[60] Han, D., Kim, H., Lee, S., Seo, M., and Yoo, S., “Realization of efficient semitransparent organic photovoltaic cells with metallic top electrodes: utilizing the tunable absorption asymmetry”, *Opt. Express*, vol. 18, pp. A513-A521, 2010.

[61] Shieh, J.-T., Liu, C.-H., Meng, H.-F., Tseng, S.-R., Chao, Y.-C., and Horng, S.-F., “The effect of carrier mobility in organic solar cells”, *J. Appl. Phys.*, vol. 107, pp. 084503-1-084503-9, 2010.

Appendix A

Table A.1. Extracted parameter values by using curve fitting method for the generation rate profiles shown in Fig. 3.9.

Fitting parameters	Fig. 3.9 (a)	Fig. 3.9 (b)	Fig. 3.9 (c)	Fig. 3.9 (d)
a_1	1.214×10^{28}	7.176×10^{27}	5.599×10^{27}	5.301×10^{27}
a_2	3.978×10^{27}	1.8×10^{27}	3.035×10^{27}	3.401×10^{27}
a_3	8.156×10^{26}	4.806×10^{26}	4.89×10^{26}	1.051×10^{26}
a_4	3.573×10^{26}	2.046×10^{26}	2.441×10^{26}	8.494×10^{25}
a_5	2.117×10^{26}	1.253×10^{26}	1.396×10^{26}	5.825×10^{25}
b_1	4.621×10^{7}	2.529×10^{7}	1.894×10^{7}	1.557×10^{7}
b_2	9.004×10^{7}	4.042×10^{7}	4.181×10^{7}	3.147×10^{7}
b_3	1.648×10^{8}	9.465×10^{7}	7.57×10^{7}	9.15×10^{7}
b_4	2.671×10^{8}	1.559×10^{8}	1.259×10^{8}	1.176×10^{8}
b_5	2.923×10^{8}	1.756×10^{8}	1.402×10^{8}	5.238×10^{7}
c_1	-0.1116	0.06018	-0.2943	-0.5401
c_2	1.928	2.081	0.8395	1.139
c_3	2.844	3.642	2.553	1.819
c_4	2.928	4.092	1.928	2.247
c_5	5.298	6.325	3.973	3.066